

The Vanadium Redox Flow Battery - Electrochemical Impedance Characterization

Joana Dias Fonseca

Thesis to obtain the Master of Science Degree in
Energy Engineering and Management

Supervisors: Prof. Alda Maria Pereira Simões
Prof. Rui Pedro da Costa Neto

Examination Committee

Chairperson: Prof. Francisco Manuel da Silva Lemos
Chairperson: Prof. Alda Maria Pereira Simões
Member of the Committee: Prof. José Armando Luísa da Silva

January 2021

Acknowledgments

I would first like to thank my supervisor prof. Alda Simões for sharing all her knowledge with me and for always trying to push me to go further and improve my skills. My sincere thanks also to prof. Rui Costa Neto, whose great enthusiasm about this topic never failed to inspire me.

I would also like to thank the institution, Instituto Superior Técnico, and all the professors that contributed to my continuous learning. A special thank you to my labmates for all the help provided, specially as someone who did not have much experience working in a lab on her own.

To all my friends who shared this journey with me I would like to thank as well, specially Pedro, who made the writing process way more fun and less lonely, even during a global pandemic.

Most importantly, I would like to thank my family not only for the financial support they provided throughout my years as a student but specially for all the emotional support. I specially want to thank my mother, who always went far and beyond to make sure I had all the conditions reunited to properly focus on my work, my father who never failed to believe in me and my brother who always knows how to keep me grounded.

Abstract

With the increasing use of intermittent renewable energy sources, such as solar and wind energy, electricity storage systems such as redox flow batteries have been the target of growing interest. In this work, the electrochemical characterization of a Vanadium Redox Flow Cell (25 cm²) was performed. Polarization curves were taken where current densities achieved 11 mA/cm² and 92 mA/cm² for an electrolyte with vanadium concentration of 0.125 M and 1.21 M, respectively. Electrochemical Impedance Spectroscopy (EIS) measurements were made for different experimental conditions to study the response of the cell. The cell's ohmic resistance for standard experimental set up and a vanadium concentration of 0.125 M was found to be 3.9 Ω cm² and 97% of it accounts for the membrane. The faradaic resistance varied with the cell's State of Charge (SOC) and ranged from 3.8 to 13 Ω cm², its lowest value at 30-70% SOC. The charge-transfer resistance increases 15.2 times with the removal of the carbon felts, and mass transport variations were also observed. The economic assessment of a VRFB installation in a "Recheio" Supermarket in Tavira was performed and the project resulted in a positive Net Present Value (NPV) of 43 247 € after 20 years.

Keywords

Vanadium Redox Flow Battery; Electricity Storage Systems; Electrochemical Impedance Spectroscopy; Economical Evaluation

Resumo

Com aumento da utilização de fontes de energia renováveis intermitentes, como a energia solar e eólica, sistemas de armazenamento de electricidade, como é o caso das baterias redox de escoamento, têm vindo a ser alvo de interesse crescente. Neste trabalho, foi realizada a caracterização eletroquímica de uma célula de escoamento de vanádio (25 cm^2). Curvas de polarização foram obtidas, nas quais foram atingidas densidades de corrente entre os 11 mA/cm^2 e 92 mA/cm^2 para um eletrólito com concentração de vanádio de 0.125 M e 1.21 M , respetivamente. Espetroscopia de Impedância Eletroquímica foi utilizada para estudar a resposta da célula em diferentes condições experimentais. Da resistência ohmica total da célula na configuração experimental padrão ($3.9 \Omega \text{ cm}^2$), 97% corresponde à sua membrana. A resistência farádica variou com o estado de carga entre $3.8 \Omega \text{ cm}^2$ e $13 \Omega \text{ cm}^2$, mostrando menor resistência para um estado de carga na gama de 30-70%. O aumento da resistência de transferência de carga com a área de superfície ativa dos elétrodos foi verificada com a remoção dos feltros de carbono, e variações no transporte de massa foram também observadas. Foi também efetuada a avaliação económica de uma instalação de uma bateria de escoamento de vanádio num Supermercado "Recheio" em Tavira e o projeto de 20 anos resultou num Valor Atual Líquido (VAL) positivo de 43 247 €.

Palavras Chave

Bateria de Escoamento de Vanádio; Sistemas de Armazenamento de Eletricidade; Espetroscopia de Impedância Eletroquímica; Avaliação Económica

Contents

1	Introduction	1
1.1	The Demand for Energy Storage Systems	1
1.2	Energy Storage Technologies	2
1.3	Electrochemical energy storage	3
1.4	State of the Art	8
1.5	Objectives and Structure of the Present Work	10
2	Vanadium Redox Flow Batteries	13
2.1	Reactions and Principles	13
2.2	The Nernst Equation and State of Charge	14
2.3	Current flow	17
2.4	Performance indicators	20
2.5	Non-ideal behaviour of VRFB	22
3	Electrochemical Techniques	27
3.1	Polarization curves	28
3.2	Electrochemical Impedance Spectroscopy	29
4	Experimental Conditions	35
4.1	Electrolyte	35
4.2	Cell Assembly	36
4.3	Testing conditions	39
5	Results and Interpretation	41
5.1	Charge-discharge cycles	41
5.2	Polarization curves	44
5.3	Electrochemical Impedance Spectroscopy	46
6	Economic Evaluation	61
7	Discussion	67
8	Conclusions	73

List of Figures

1.1	Peak load shaving using battery energy storage systems (BESS).	2
1.2	Schematic illustration of a redox flow battery [1].	6
1.3	Schematic illustration of a Vanadium redox flow battery [2].	7
3.1	Generalized polarization curve for a VRB indicating the dominant source of overpotential in each region [3].	28
3.2	Example of a Nyquist Plot for a simple RC parallel circuit. $R=10\ \Omega$; $C=0.005\ \text{F}$	30
3.3	Example of a Bode plot for simple RC parallel circuit. $R=10\ \Omega$; $C=0.005\ \text{F}$	31
3.4	Schematic idealized impedance complex plane plot for a VRFB cell [4]	32
4.1	Schematic of the assembly of the cell.	37
4.2	Fully assembled VRFB cell.	38
4.3	VRFB set-up for experimental measurements.	38
5.1	Charge-discharge curves for the current densities of 4, 8 and $12\ \text{mA/cm}^2$, with stagnant electrolyte at a concentration of 0.125 M.	42
5.2	Evolution of cell potential with SOC, for a formal potential of 1.43 V, $T=298\text{K}$, calculated from Equation (2.2.11).	44
5.3	Discharging polarization curves for a concentration of 0.125 M at different flow rates, with a scan-rate of 2 mA/s.	45
5.4	Discharging polarization curves for a concentration of 1.21 M at different flow rates, with a scan-rate of 2 mA/s.	45
5.5	Polarization curves at a flow rate of 16.1 mL/min for different vanadium concentrations, 1.21 M and 0.125 M, with a scan-rate of 2 mA/s.	46
5.6	Impedance spectrum for the VRFC with a vanadium concentration of 0.125 M, electrolyte flow rate 24.1 mL/min, at the cell's spontaneous potential.	47

5.7	Fitting results directly taken from ZView Software for a vanadium concentration of 0.125 M, flow rate 24.1 mL/min, DC polarization 0 mV using a circuit model with 2 RC networks in series with a resistor and a CPE, where units for R are $\Omega \text{ cm}^2$, for CPE-T are $\text{F cm}^{-2}\text{s}^{\alpha-1}$, and CPE-P has no units. $\chi^2 = 9.9 \times 10^{-5}$	48
5.8	Fitting results directly taken from ZView Software for a vanadium concentration of 0.125 M, flow rate 24.1 mL/min, DC polarization 0 mV, using a circuit model with 3 RC networks in series with a resistor, where units for R are $\Omega \text{ cm}^2$, for CPE-T are $\text{F cm}^{-2}\text{s}^{\alpha-1}$, and CPE-P has no units. $\chi^2 = 6.7 \times 10^{-5}$	48
5.9	Nyquis and Bode plots obtained at a vanadium concentration of 0.125 M having carbon felts in both half-cells, only in the negative half-cell and no carbon felts at all.	49
5.10	Impedance spectra of the VRFC with the setup using single or multiple Nafion membranes; flow rate 20.4 mL/min, concentration 0.125 M.	50
5.11	Fitting result directly taken from ZView Software for the Nyquist plot obtained for one membrane, where units for R are $\Omega \text{ cm}^2$, for CPE-T are $\text{F cm}^{-2}\text{s}^{\alpha-1}$, and CPE-P has no units.	50
5.12	Evolution of the high frequency resistance with the number of membranes.	51
5.13	Impedance spectra of the VRFC obtained for different levels of SOC; vanadium concentration of 0.125 M and flow rate of 20.4 mL/min.	52
5.14	Impedance spectra of the VRFC obtained for different levels of SOC; vanadium concentration of 0.125 M and stagnant electrolyte.	52
5.15	Fitting directly taken from ZView Software for the experimental results at 16% SOC for a vanadium concentration of 0.125 M (flow rate of 20.4 mL/min), where units for R are $\Omega \text{ cm}^2$, for CPE-T are $\text{F cm}^{-2}\text{s}^{\alpha-1}$, and CPE-P has no units.	53
5.16	Evolution of R_2 with SOC with and without electrolyte circulation.	54
5.17	Impedance spectra of the VRFC with and without carbon felts; vanadium concentration of 1.21 M and flow rate of 20.4 mL/min.	55
5.18	Fitting results directly taken from ZView Software for a cell with carbon felts (concentration of vanadium 1.21 M, flow-rate 20.4 mL/min), where units for R are $\Omega \text{ cm}^2$, for CPE-T are $\text{F cm}^{-2}\text{s}^{\alpha-1}$, CPE-P has no units.	55
5.19	Fitting results directly taken from ZView Software for a cell without carbon felts (concentration of vanadium 1.21 M, flow-rate 20.4 mL/min), where units for R are $\Omega \text{ cm}^2$, for CPE-T are $\text{F cm}^{-2}\text{s}^{\alpha-1}$, CPE-P has no units, $W_o\text{-R}$ has units of $\Omega \text{ cm}^2 \text{ s}^{-0.5}$, $W_o\text{-T}$ has units of s and $W_o\text{-P}$ has no units.	56

5.20 Impedance spectra of the VRFC with and without carbon felts, after applying a multiplier of 15.2 to "with felts" impedance and subtracting a 74.6 Ω resistor; vanadium concentration of 1.21 M and flow rate of 20.4 mL/min.	57
5.21 Impedance spectra of a VRFC for vanadium concentrations of 0.125 M and 1.21 M; flow rate of 20.4 mL/min.	58
5.22 Values of R_0 , R_1 and R_2 for vanadium concentrations of 0.125 M and 1.21 M.	58
5.23 Graphite plates with (a) and without (b) corrosion and particles removed by the tape from the corroded electrode (c) and the non-corroded electrode (d).	59
5.24 Impedance spectra obtained before and after overcharging the cell; 45% SOC and flow rate of 20.4 mL/min.	60
5.25 Fitting results directly taken from ZView Software for a 45% SOC after overcharging the cell at 2.2 V, where units for R are $\Omega \text{ cm}^2$, for CPE-T are $\text{F cm}^{-2} \text{ s}^{\alpha-1}$, and CPE-P has no units.	60
6.1 Typical load curve and solar production curve for summer and winter months. Power demand during the winter was considered to be 20% lower in comparison with summer. .	62
6.2 Power demanded to the grid during a) summer and b) winter when a VRFB is and is not installed.	64

List of Tables

5.1	Total charge and Coulombic Efficiency for the different current densities.	42
5.2	Data gathered to assess the formal potential of the cell.	43
6.1	Properties for each type of battery.	63
6.2	Economic parameters calculated for each BESS technology.	66

Acronyms

BESS Battery Energy Storage Systems

DoD Depth of Discharge

CE Coulombic Efficiency

CE Cyclic Voltammetry

CPE Constant Phase Element

EE Energy Efficiency

EIS Electrochemical Impedance Spectroscopy

ESS Energy Storage Systems

EV Electric vehicles

GCD Galvanostatic charge-discharge

HER Hydrogen Evolution Reaction

IRR Internal Rate of Return

LIB Lithium-ion battery

OCP Open Circuit Potential

OER Oxygen Evolution Reaction

PHES Pumped Hydro Energy Storage

PTFE Polytetrafluoroethylene

PV Photovoltaic systems

NPV Net Present Value

RES Renewable Energy Sources

RFB Redox Flow Battery

ROI Return on Investment

SOC State of Charge

VRFB Vanadium Redox Flow Battery

1

Introduction

1.1 The Demand for Energy Storage Systems

In a world where environmental consequences from human activities are already greatly felt by society, new emerging technologies must focus on sustainable ways in which we can keep evolving without taking a toll on our planet. Some of these technologies include the ways we explore the different energy sources, namely renewable energy sources (RES) like wind and solar that allow us to significantly reduce the amount of CO₂ released to the atmosphere during electricity production. The problem with these sources, as opposed to traditional ones like coal and petroleum, is their intermittent nature, which makes them less reliable in terms of guaranteeing fulfilment of power demand at all times. This is where efficient energy storage systems (ESS) become necessary.

Although renewable energy sources like the wind and the sun are essentially free, which makes them very economically attractive in the long-run even with the high investment costs inherent, it is also true

that the lack of cost-effective storage technologies can become an issue. In times where power generation actually exceeds power demand (like sunny afternoons or very windy hours), not having ESS would result in loss of energy and the grid's efficiency would decrease. Using ESS to store energy produced in times where power generation exceeds demand for peak shaving during times where the opposite occurs helps us improve efficiency [5]. A schematic representation of how peak shaving works for solar energy can be found in Figure 1.1, where it is seen that battery energy storage systems (BESS) can be charged when the electricity production exceeds the demand, in the middle of the day, and the stored energy can later be used when no radiation is available to give response to the electricity demand. Energy storage systems are also useful to guarantee power quality, making use of highly responsive devices that smooth power delivery during switching events, short outages, or plant run-up [6]. ESS are also used, of course, for energy portability, for example, in electric vehicles (EV) or portable electronics such as mobile phones.

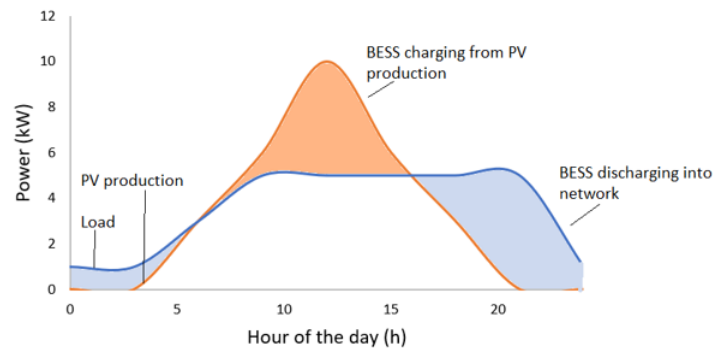


Figure 1.1: Peak load shaving using battery energy storage systems (BESS).

1.2 Energy Storage Technologies

Energy storage can be defined as the capture of energy produced at one time for use at a later time. Energy in forms that are difficult to store, such as electricity or kinetic energy, can be converted to more conveniently or economically storable forms, such as chemical or potential energy, so that they can be stored away [7]. Different types of energy storage systems are already known, making use of different technologies, which are presented below.

Mechanical energy storage

Energy is commonly stored in the form of potential energy. This is most commonly seen in hydro-pump

facilities. Pumped-hydro energy storage (PEHS) facilities represent the energy storage system with the highest capacity exploration this far in our world [8]. This system uses potential energy as the "storage medium". Electrical energy is used to push the water upstream, which is then stored in the upper reservoir. When the water is released with all its potential energy, the turbines become generators able to transform kinetic energy into electrical energy [9]. Big issues regarding this technology are related to its ecological impact. Pumped storage hydropower systems need to be installed in locations with specific conditions, such as elevated ground with access to water. Only a limited number of places can be exploited in this sense. The biggest drawback of these installation is the natural landscape transformation, which in some countries is also attached to the relocation of populations [10].

Electrical energy storage

A capacitor stores energy in the electric field between two oppositely charged conductors. The ultracapacitor or supercapacitor differs from traditional capacitors in the sense that it employs a thin electrolyte instead of a dielectric between the two conducting plates, thus increasing the energy density of the device. However, ultracapacitors remain as high power density systems, with moderate energy density. They are, therefore, mostly used for intense yet short applications, such as regulating voltage in automotive systems during regular driving conditions [6].

Thermal energy storage

In this technology, thermal energy is used during day time to melt salts or other materials that can be stored in the liquid form above 100 °C, and during the evening the stored heat generates steam for power production. Alternatively, off-peak electricity generation can be converted into thermal energy by Joule heating, and then get converted back into electricity using a Rankine cycle [11].

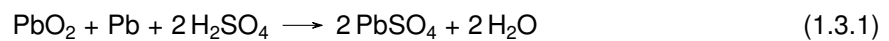
1.3 Electrochemical energy storage

Chemical energy storage systems are mostly seen in the form of electrochemical batteries, in which electrical energy is produced from chemical energy (or vice-versa, if they are rechargeable). The principles behind the concept of electrochemical batteries rely on redox chemical reactions to create an electromotive force. A negative electrode, in which oxidation occurs, gives up electrons to an external load and a positive electrode, where reduction occurs, accepts those electrons [6]. There are different

designs for electrochemical energies, using different electroactive species. The fast response, allied to the high level of maturity of diverse types of electrochemical energies, makes them the preferred method of storage for many applications, from stationary to mobile.

Lead-acid batteries

Lead-acid batteries have been market leaders for the last decades. The positive electrode consists of porous lead dioxide and the negative electrode is finely divided lead [12]. During discharge, both electrodes result in lead sulfate formation, as seen in:



Their most common applications are for automotive batteries or industrial batteries, specially to provide secure standby power in telecommunications and huge data networks [12]. The great advantage of lead-acid batteries lies on their low cost of installment (206 €/kWh [13]), as well as good storage efficiency of 85% [12, 14]. These batteries can also reach 100% rates of recycling [15], which stands out from other competitors. Some drawbacks include the low number of cycles (2000) in its life cycle (10 years) [12]. Furthermore, they show limited energy density (37 Wh/kg [9]), and the lead production/use brings several well-known environmental concerns.

Lithium-ion batteries

Lithium-ion batteries (LIB) have become incredibly popular over the last decade. They're based on the migration of lithium ions from anode to cathode and vice-versa, while compensating electrons travel in the external circuit. Different chemistries can be used, but a layered structure at the electrodes allows the flow of lithium ions over several cycles. The cathode is usually composed by a mixture of nickel, cobalt, aluminum and manganese, while the material used for the anode is often graphite [16]. Reactions at the anode and cathode, respectively, are as follows:



The most valuable feature of lithium-ion batteries is their high energy density (up to 200 kWh/kg), which

makes them highly suitable for mobile applications, such as portable electronics or electric/hybrid vehicles [17]. They also show high voltage per cell (3.7 V), which means that a single cell might be enough to run a mobile phone [7]. While nickel at the cathode provides good energy density, the cobalt is essential for the layered structure. However, cobalt is a scarce raw material which is mostly found in the Democratic Republic of Congo, a country with a very unstable economy. Moreover, with the anticipated increase in demand for these batteries for EV and other electronics, manufacturers fear that the demand for cobalt will outstrip its production in the next decade. These aspects have made researchers focus their attention on finding new cobalt-free approaches for Li-ion batteries' cathodes[18]. Another issue related to Li-ion batteries is their safety. The materials they are made of are highly flammable and reactive, and many explosions and fire accidents have been reported [19]. It is important to perform good thermal management to these batteries to avoid safety issues. Even though these batteries are more expensive (288 €/kWh [13]) than lead acid batteries, their efficiency (93% [20]) and increased number of cycles (2500 cycles [12]) make them another suitable approach to be used for utility energy storage on a stationary level. Moreover, costs are believed to significantly decrease in the upcoming years [12].

In the hope to find electrochemical storage systems that reduce the environmental and practical issues that may arise with the current systems, researchers all over the world keep exploring new technologies.

Redox Flow Batteries

Redox Flow Batteries (RFB) have recently raised the attention of new researchers as a new interesting concept. They fall into a specific type of electrochemical batteries in which the electrolyte containing the diluted redox couple is stored outside the cell and gets circulated by pumps through the cell's inert electrodes, where the electroactive species are oxidized or reduced. The cell is composed by two compartments separated by an ion-exchange membrane which serves as a charge-carrier conductor while preventing the electrolytes of the two sides from mixing. The general scheme of a RFB can be seen in Figure 1.2. To form an operational battery, 10–200 cells can be combined in stacks [21].

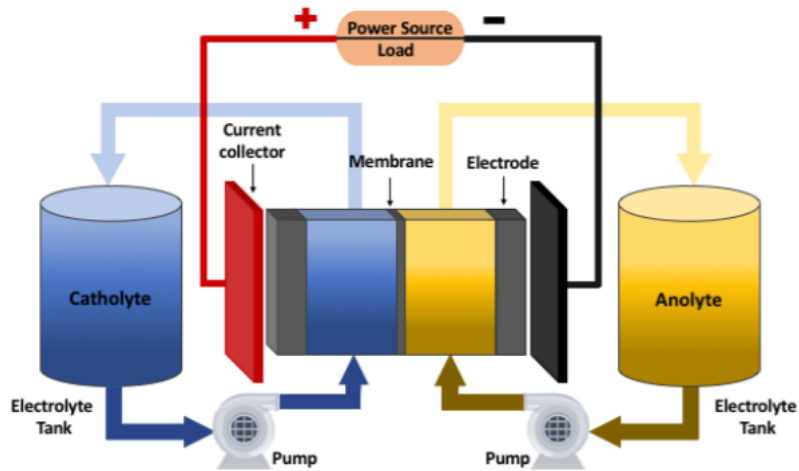


Figure 1.2: Schematic illustration of a redox flow battery [1].

Several combinations of electroactive species have already been tested for RFB applications. We can divide RFB into two broad categories: hybrid phase and all-liquid batteries. Hybrid phase systems consist of gas/liquid, solid/liquid and semi-solid phases. All-liquid systems differ from conventional batteries as the reactions take place in the electrodes that do not take an active role in them [22]. The reactions occur between two dissolved species, rather than between a dissolved species and an electrode [9].

Due to their unique characteristics, RFB are often referred to as reversible fuel cells [23]. With the electrolyte being stored externally from the cell, the charging of the cell can be done either by applying a potential to the cell's terminals, forcing the charging reaction to occur, or replacing the discharged electrolyte with a new charged one.

In RFB, the power and the energy capacity of the system are independent. The cell's capacity is directly related to the number of active species available to react and transfer electrons, which in the case of a RFB depends upon the size of the electrolyte container or the concentration of active species, which is independent of the size of the cell itself. The power of the system is determined by the number of cells in the stack and the size of the electrodes. It is therefore possible to scale up the cell's capacity without significantly change its size.

Apart from the advantages mentioned, RFB also become attractive due to the simplicity of their reactions, their high life-cycle no problems in deep discharge of the system [21]. RFB have so far been considered for large stationary applications, ranging from a few kW to MW, but smaller systems can also

be envisaged [9].

Early concepts of RFB were first proposed by the U.S. National Aeronautics and Space Administration (NASA) in the 1970s, using $\text{Fe}^{3+}/\text{Fe}^{2+}$ and $\text{Cr}^{3+}/\text{Cr}^{2+}$ redox couples in the positive and negative half-cells, respectively. The crossing-over of species through the membrane contaminates the electrolyte and may lead to irreversible reactions that compromise the cell's efficiency, degrading the overall performance of the system [23, 24]. The idea of using the same element with different oxidation states on both sides of the RFB then came about and the All-Vanadium Redox Flow Batteries (VRFB) were first proposed in 1987 by Skyllas-Kazacos et al from the University of New South Wales in Sydney, Australia.

In VRFB, the active species are Vanadium molecules in four different states of oxidation (II, III, IV and V). A redox couple of $\text{V}^{2+}/\text{V}^{3+}$ can be seen in one half-cell where, in discharge, there is the oxidation of V^{2+} to V^{3+} (anode) with the release of an electron which will flow through the current collectors and wires and be consumed at the positive electrode, in the other half-cell, where we find the $\text{V}^{4+}/\text{V}^{5+}$ couple and V^{5+} gets reduced to V^{4+} .

The general scheme of a VRFB can be seen in Figure 1.3. The two half-cells are separated by a membrane, which allows the transport of protons to complete the circuit between the two half-cells without, ideally, enabling the cross-over of other ions. In a VRFB, the cross-over of vanadium cells does effect negatively the overall capacity and efficiency of the system, but will not result in irreversible contamination that would otherwise occur and result in big costs for electrolyte separation and reactant recovery [24].

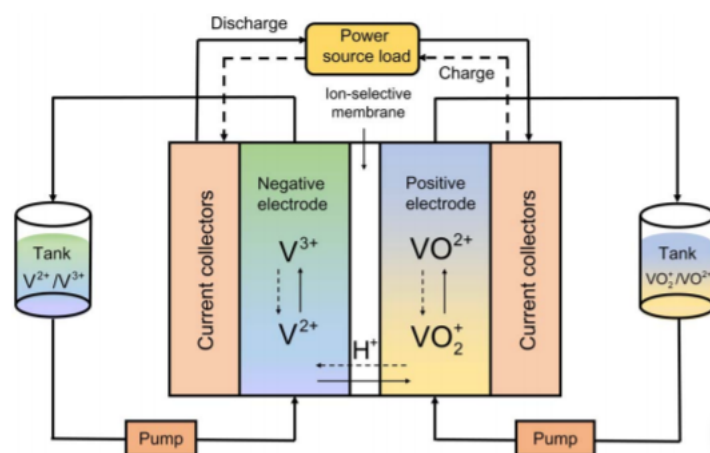


Figure 1.3: Schematic illustration of a Vanadium redox flow battery [2].

The electrolyte is an aqueous acidic solution. Vanadyl sulphate (VOSO_4) is typically used to prepare the solution with sulfuric acid, although it can be replaced by other compounds, such as vanadium pentoxide (V_2O_5), to lower the manufacturing costs of the battery. Vanadium pentoxide presents, however, lower solubility, making it difficult to achieve high concentration solutions [25, 26]. Electrolytic reduction and oxidation can be used to attain the desired ions in specific oxidation states. The solution will remain strongly acidic.

VRFB is considered an environmentally friendly energy storage technology, as it does not involve toxic substances. The electrolyte can be, in theory recycled (recharged) indefinitely, and even in the case of replacement with fresh electrolyte, it does not contain any aggressive chemicals that will harm the environment. Vanadium is also a particularly abundant element in the planet, even though extraction remains costly [27]. One of the major drawbacks of this technology, however, is its energy density, which is low compared to other electrochemical batteries. Vanadium presents low solubility in aqueous solutions, which makes it hard to increase the energy available in the cell, that is, the number of active species, without significantly increasing its volume as well. A VRFB would present a poor specific energy of 20-25 Wh/kg compared to 37 Wh/kg for the lead-acid battery [9]. In terms of round-trip efficiency, VRFB shows only 75% [28]. More details about the electrochemistry of VRFB will be presented in Chapter 2.

1.4 State of the Art

ESS have become crucial in the RES upgrowth not only due to peak shaving purposes but also to provide stable and reliable voltage and frequency in power [17]. This is most important in isolated systems where the size of the power transmission and distribution grid makes the intermittent nature in energy production have more severe consequences. In islands, for example, weather and geographical conditions are often suitable for installation of RES, but they need to be combined with some sort of ESS.

Pumped hydro energy storage represents, as we have seen, a great option when it comes to dealing with the intermittent nature of RES. In fact, its application in different sites such as the Greek islands, Azores and Corsica (France) has been investigated by several authors [29, 30, 31]. While islands may be suitable for PHES installations, geographical limitations may undermine this technology's success in the mainland, specially given the increase in ESS demand predicted to occur in the upcoming years.

This is where battery energy storage systems play an important role, being lead-acid batteries, Li-ion batteries and VRFB the key solutions.

Lead-acid batteries are specially competitive due to their maturity level, low cost of installment and high rate of recycling. These batteries have been used in utility storage long before RES arrived to the scene, mainly for frequency regulation. In 2012, the whole King Island in Tasmania, Australia benefited from a 3 MW/1.6 MWh UltraBattery lead acid battery system installation, from the company Ecoult, which was able to power the entire island for up to 45 minutes [32].

Although lithium-ion batteries are widely used in portable devices due to their high energy density, they have flexibility to be deployed also for large-scale storage [30]. In fact, LIB prices are expected to fall in the following years, so much that it makes difficult for other technologies to penetrate the market [33, 34]. In the USA, 77% of the electrical power storage relies on LIB. In 2010, a system with 8 MW/2 MWh was installed and then increased to 16 MW in New York for frequency regulation services. Specifically for RES peak shaving, a 32 MW/8 MWh system was installed in Pennsylvania to support the 98 MW wind generation. The largest system installed in Europe is in the UK, with a power of 6 MW/10 MWh. In Japan, a project was launched by Toshiba to install a 40 MW/20 MWh LIB system in Tohoku [17].

When it comes to redox flow batteries, VRFB are the ones being commercialized to a larger extent so far. With their low energy density, the only possible application for this technology would be in stationary projects. They are mostly used for utility storage or commercial and industrial facilities trying to lower their electricity bills [35]. In spite of the fact that the big developments started in Australia and the technology was patented to the University of New South Wales [36] for a period of time, nowadays it is already commercialized and exploited in several countries, although in limited scale. In Europe, the interest for load levelling and power quality was small for many years, which can be due to the already efficient, nationally interconnected, high voltage transmission system. Nevertheless, in Ireland, 2006, VRB Energy completed the installation of 1.5 MW/12 MWh flow battery at the 38 MW Sorne Hill Wind farm in County Donegal [37]. In 2008 the production of a 100 kWh capacity flow battery was started in Austria, for sale within Europe only and meant to supply commercial installations or apartment blocks [9]. In Japan, a 17MW / 51MWh VRFB system is being installed by Sumitomo Electric in the island of Hokkaido. In the same region, the world's biggest flow battery from the same company had already been deployed, with a 60 MWh capacity [27]. Another big company with projects worldwide is VRB Energy, from Canada, that claims to have developed the most reliable, longest-lasting VRFB. They are taking part in the big 100MW 500MWh energy storage project that will be the cornerstone of a new smart energy grid in Hubei Province, China, where VRFB will not be the only ESS installed [38]. In California,

the USA based company Invinity is installing a 7.8MWh VRFB system to perform a range of services including peak shaving, demand charge reduction, and provision of back-up power [39]. Apart from the all-vanadium flow batteries, zinc-bromine flow batteries are also being commercialized by RedFlow for commercial and industrial applications, mostly in Australia [40].

According to Deloitte's report in 2015, redox batteries and hydrogen technology are expected to become the leader ESS when it comes to renewables integration by 2030 [41]. On the other hand, other studies [42] evaluate the maturity level of VRFB as too low, identifying some challenges to the technology such as low energy density, electrolyte leakage protection requirements and high costs of installment.

It is important to consider that a wide variety of costs have been one of the major contributors for the slow rate of commercialization of the VRFB technology. The total costs of manufacture depend, of course, of its specifications. It will vary with capacity and power. Costs of manufacture can be related to the necessary chemicals, membrane, bipolar plates, electrode felts and other components such as pumps, frames and bolts. Analysis have shown that for a 0.25 MWh system the membrane and chemicals account for 27% and 22% respectively, if the cost of the power conversion system is disregarded. For a 4 MWh system, on the other hand, chemicals account for 58% of total costs, which would be 274 €/kWh [43]. Sensitivity analysis has shown that normal changes in vanadium costs will result in big changes in capital costs. Using vanadium costs near that of the lowest grade vanadium will be necessary to keep the capital costs of the VRFB down [44]. Although vanadium is much more abundant than lithium in this world, its extraction is what makes it so expensive. However, VRFB remain safer, more scalable and longer-lasting than LIB, which is what makes them competitive [27]. Further studies about this relatively new technology will help improve its efficiency and possibly reduce its manufacture costs, which is what ultimately inspired this work.

1.5 Objectives and Structure of the Present Work

With its increasingly important role in today's society, it becomes crucial to understand the behavior of ESS like VRFB and explore their performance in the best way. It is also important to find new ways to minimize the costs of manufacture for this technology, as this remains as the main drawback keeping this technology to out stand the others. The Laboratory of Corrosion Science and Surface Engineering of Instituto Superior Técnico from the University of Lisbon has developed a vanadium redox flow cell with the use of simple and low-cost materials [45]. The aim of this work is to perform the electrochem-

ical characterization of said cell, through different techniques and giving a special emphasis into the interpretation of Electrochemical Impedance Spectroscopy results.

This thesis is organized as follows: Chapter 1 has given an introduction about the topic, and the good perspective of how developed the technology of VRFB already is. In Chapter 2 more details will be given about the electrochemistry of VRFB, their properties and some performance metrics that can be used to evaluate them. In Chapter 3 some techniques for electrochemical characterization of a cell are discussed, to present a theoretical background about the methods applied in the experimental part of this work and better understand the results. Chapter 4 will discuss the experimental methods used and Chapter 5 will present the results. The economic evaluation of installing a VRFB system in a commercial facility will be presented in Chapter 6. Both results from the electrochemical characterization and the economic evaluation will be discussed in Chapter 6. Finally, in Chapter 8, conclusions will be drawn and some perspectives for future work will be presented in Chapter 9.

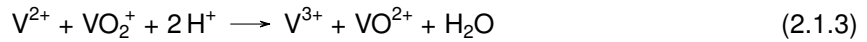
2

Vanadium Redox Flow Batteries

2.1 Reactions and Principles

As mentioned in Chapter 1, VRFB reactions involve only vanadium ions in different oxidation states as active species. Vanadium exists in aqueous solution in four different oxidation states. While V^{2+} and V^{3+} are seen in solution in their simple form, V^{4+} and V^{5+} are seen in the form of the poliatomic ions VO^{2+} and VO_2^+ , respectively. The supporting electrolyte is sulfuric acid 1-3 M or above, and concentrations of vanadium are usually in the range of 1-2 M [23]. The reactions taking place during discharge for the anode and cathode become, respectively:





The anolyte thus contains V^{2+} and V^{3+} in solution, whereas the catholyte contains VO^{2+} and VO_2^+ species. During discharge mode, the anolyte is pumped through the cell and the V^{2+} ions react at the inert graphite electrode, getting oxidized into V^{3+} with the release of one electron, while on the other half-cell VO_2^+ is reduced to VO^{2+} . Hydrogen cations are produced or consumed during the charge-discharge cycles and their transit across the membrane assures the charge balance between both half-cells [23].

A curious feature about vanadium is its change of color throughout the different oxidation states. For the usual conditions of pH and vanadium concentration, a V^{2+} solution will present a purple color, while a V^{3+} will be marine green, a V^{4+} blue and V^{5+} yellow [46].

The standard reduction potential E° is a thermodynamic parameter that measures the individual potential of any electrode at standard conditions: 25 °C, 100 kPa and solutes at a concentration of 1 M. With the standard reduction potential for the anode and cathode reactions being -0.26 V and +1.0 V, respectively, the standard potential for the cell becomes 1.26 V. This is the potential at concentrations 1 M at 25 °C:

$$E_{cell}^\circ = E_{cathode}^\circ - E_{anode}^\circ = 1.26\text{V} \quad (2.1.4)$$

2.2 The Nernst Equation and State of Charge

Standard conditions are often not the conditions we operate in, and consequently the equilibrium potential will not be the same as the standard electrode potential. Willard Gibbs stated that the maximal amount of energy that can be extracted from a chemical reaction is given by the available energy, now called in his honor the Gibbs free energy ΔG :

$$\Delta G = \Delta H - T\Delta S \quad (2.2.1)$$

where ΔH is the change in enthalpy, T is the system's temperature and ΔS the change in entropy. Conservation of energy then relates the change in free energy with the transfer of n moles of electrons and the difference of potential E [47]:

$$\Delta G = -nFE \quad (2.2.2)$$

where F is the Faraday constant. Thermodynamics will also tell us that:

$$\Delta G = \Delta G^\circ + RT \ln K \quad (2.2.3)$$

where R is the gas constant and K stands for the equilibrium constant. ΔG° is the variation in the Gibbs free energy in standard conditions. Combining Equation (2.2.2) and Equation (2.2.3), we finally get the Nernst equation, which allows us to know the equilibrium potential of an electrode for its specific conditions of temperature, pressure and concentration of solutes:

$$E_{eq} = E^\circ - \frac{RT}{nF} \ln K \quad (2.2.4)$$

where n is the number of electrons transferred in the reactions. With Equation (2.1.4) and Equation (2.2.4), the VRFB's equilibrium cell potential can be computed by the following equation, knowing that only one electron is transferred in both reactions:

$$E_{eq} = 1.26 + \frac{RT}{F} \ln \frac{(VO_2^+)(V^{2+})(H^+)^2}{(V^{3+})(VO^{2+})} \quad (2.2.5)$$

The notation (X) represents the activity of the agent X in the solution. The activity of each agent is given by the product of its concentration in solution and its respective activity coefficient γ , as seen in the example below:

$$(V^{2+}) = [V^{2+}]\gamma_{V^{2+}} \quad (2.2.6)$$

When the concentration of solutes is sufficiently small, the activity coefficient can be taken as one, but for the range of concentrations in which VRFB operate the activity coefficient should not be neglected. The activity coefficients are, however, difficult to measure. The Nernst equation also includes the concentration of hydrogen cations, which is difficult to assess given the reactions occurring during charging and discharging in the positive half-cell and the crossover of protons through the membrane [48]. To tackle these obstacles, one can use the concept of formal potential $E^{\circ'}$, which depends on experimental conditions and can be measured empirically.

$$E^{\circ'} = E^\circ + \frac{RT}{F} \ln \frac{\gamma_{VO_2^+}\gamma_{V^{2+}}(H^+)^2}{\gamma_{V^{3+}}\gamma_{VO^{2+}}} \quad (2.2.7)$$

This way we get the final equation for the equilibrium potential of the cell.

$$E_{eq} = E^{\circ} + \frac{RT}{F} \ln \frac{[VO_2^+][V^{2+}]}{[V^{3+}][VO^{2+}]} \quad (2.2.8)$$

Equation (2.2.8) is important to assess the cell's State of Charge (SOC). The SOC accounts for how much of the battery's full capacity is still available to perform. A fully charged battery should present a SOC of 1, while an uncharged battery should present a SOC of 0. The SOC can be translated by the number of reduced species in relation to the number of total species, reduced and oxidized, inside the anolyte. In the same way, it can be translated by the number of oxidized species inside the catholyte in relation to total amount of species. Assuming a fully balanced cell, its SOC can be computed by the following expression:

$$SOC = \frac{[V^{2+}]}{[V^{2+}] + [V^{3+}]} = \frac{[VO_2^+]}{[VO_2^+] + [VO^{2+}]} \quad (2.2.9)$$

It is easy to see how the cell's equilibrium potential and its SOC are both dependent on the concentration of the different vanadium ions. Taking Equation (2.2.9) and Equation (2.2.8) it is also possible to relate these two important properties of the cell:

$$E_{eq} = E^{\circ} + \frac{RT}{F} \ln \frac{SOC^2}{(1 - SOC)^2} \quad (2.2.10)$$

Which becomes:

$$E_{eq} = E^{\circ} + \frac{2RT}{F} \ln \frac{SOC}{1 - SOC} \quad (2.2.11)$$

It is also interesting to get the cell's SOC knowing its equilibrium potential, which can be done with:

$$SOC = \frac{\exp\left(\frac{F}{2RT}(E_{eq} - E^{\circ})\right)}{1 + \exp\left(\frac{F}{2RT}(E_{eq} - E^{\circ})\right)} \quad (2.2.12)$$

When SOC=0.5, Equation (2.2.11) then becomes $E = E^{\circ}$. By experimentally measuring the equilibrium potential of the cell when it is at 50% of its full capacity, it is possible to know the value of its formal potential for the given conditions and from then on SOC and equilibrium potential of the cell can always be found out from each other. Typical values of formal potential for the VRFB are close to 1.4 V [49]. It can be observed that, apart from the activity coefficients that should not vary too much anyway, the overall vanadium concentration of the electrolyte does not affect the Nernst equation or the relationship between equilibrium potential and SOC. Under the same conditions, cells with different vanadium concentration should have the same potential for the same SOC. The acid concentration, however, can influence the formal potential and, consequently, change the relationship.

2.3 Current flow

Until now, all the chemistry was discussed under equilibrium conditions, which are only met when there is no current flowing, so the equilibrium potential is often times also called the open-circuit potential (OCP). To have current flowing, it is necessary to apply an overpotential which represents the energy required to force the redox reaction to proceed at the required rate [9]. Applying a positive overpotential means to apply a voltage higher than the OCP, and the result will be a charging current. If the overpotential is negative, it is as if a load resistor was connected to the terminals, and there is discharging current. This phenomenon can be called polarization and can be seen in different types.

The overpotential needed to reach a certain current density is controlled by the charge transfer limiting process of the cell, unable to match the others [47]. In any electrochemical cell we can consider three types of charge transfer effects: the current of electrons flowing across electronic conductors such as electrodes, current collectors and wires; the ionic flow inside the electrolyte; and the charge-transfer occurring during reaction at the electrode/electrolyte interface.

In each half-cell there is an electrode in which both anodic and cathodic currents are present. If the system is in equilibrium, both anodic and cathodic currents will have the same rate, therefore the net rate will be zero.

$$i = i_c - i_a \quad (2.3.1)$$

When you apply an overvoltage to the system, whether it be positive or negative, the oxidation reaction in one half-cell and the reduction reaction in the other or vice-versa will be favoured, and the net current is no longer zero. To sum up, some sort of polarization in the cell is needed for the reactions to occur and the current to flow.

Studying the polarization behaviour of the cell tells us much about its performance. The polarization phenomena can also be seen as "losses" of power, because a higher voltage is required to reach a certain level of current density. These losses are associated with all the processes occurring in the cell that involve charge transfer. In the electrode we find the activation overpotential necessary for the redox reaction to take place at a certain rate and the concentration overpotential related to the difference in concentrations near the surface of the electrode and the bulk of the solution. The ohmic overpotential translates to the resistance in charge flow present in all the materials that constitute the cell, accounting for the resistivity of the wires, the electrodes, or even the ionic resistance inside the electrolyte. At any

point, the overall overpotential of the cell will be the sum of the three overpotentials.

$$\eta = \eta_{act} + \eta_{conc} + \eta_{ohm} \quad (2.3.2)$$

Activation overpotential

In a battery, the magnitude of the available current can be determined by the rate of electron transfer between the reactants in the electrodes. As we have seen before, in each electrode there are both anodic and cathodic reactions. The rate at which each of them occurs can be expressed by the following equations:

$$i_c = k_c F A [Ox] \quad (2.3.3)$$

$$i_a = k_a F A [Red] \quad (2.3.4)$$

where k_c and k_a are the rate constants, A is the area of the electrode/solution interface and $[Ox]$ and $[Red]$ are the surface concentrations of the electroactive species. The rate constants have the form:

$$k_c = k_o \exp \frac{-\alpha F (E - E^0)}{RT} \quad (2.3.5)$$

$$k_a = k_o \exp \frac{(1 - \alpha) F (E - E^0)}{RT} \quad (2.3.6)$$

where E is the potential of the electrode, E^0 its standard equilibrium potential and k_o is the single heterogeneous rate constant characteristic of the redox system at the temperature of interest. α is a constant between 0 and 1, known as the transfer coefficient or symmetry factor and its value is generally close to 0.5.

The activation overpotential, represented by η_{act} and when this is the only overpotential occurring, is the difference between the applied potential and the equilibrium potential, assuming a positive overpotential:

$$\eta_{act} = E - E_{eq} \quad (2.3.7)$$

Using the previous expressions and recalling the Nernst equation Equation (2.2.4) we get the Butler-Volmer equation:

$$i = i_0 \left[\exp \frac{-\alpha F \eta_{act}}{RT} - \exp \frac{-\alpha F \eta_{act}}{RT} \right] \quad (2.3.8)$$

In Equation (2.3.8) i is actually the current density, which is the current normalized to the active area of the electrode, i/A . This equation helps us better understand the relationship between the current density

and the overvoltage η necessary if the system is only controlled by activation. If the voltage is positive, the net reaction will be anodic, an oxidation, whereas for a negative overpotential we will see a net cathodic reaction, a reduction.

For small enough values of overpotential (≤ 10 mV) the polarization is linear, as we can see from Taylor MacLaurin expression:

$$i = i_0 \frac{\eta_{act} F}{RT} \quad (2.3.9)$$

For high overpotential ranges, the reaction will have a preferable direction and the relationship current-overpotential will be given by the Tafel Equation. For a positive overpotential, where the anodic reaction is predominant:

$$\eta = 2.303 \frac{RT}{\alpha_0 F} \log \frac{i_a}{i_0} \quad (2.3.10)$$

And for a negative overpotential, cathodic current, we have:

$$\eta = -2.303 \frac{RT}{\alpha_R F} \log \frac{i_c}{i_0} \quad (2.3.11)$$

Concentration overpotential

Concentration overpotential occurs when the concentration of active species at the interface electrode/electrolyte is not the same as the one in the bulk of the solution.

$$\eta_{conc} = \frac{RT}{nF} \ln \frac{[Ox]_0}{[Red]_0} - \frac{RT}{nF} \ln \frac{[Ox]}{[Red]} \quad (2.3.12)$$

where $[Ox]_0$ and $[Red]_0$ are the concentration of oxidizing and reducing agents adjacent to the electrode interface and $[Ox]$ and $[Red]$ are the concentrations in the bulk of the solution.

Differences between the two concentrations occur when the rate of reaction is so fast that there is not enough time to replenish the electrode surface with active species before they get depleted. In this situation, the diffusional mass transfer process becomes the limiting process for the current. Although there are other types of mass transfer processes like convection and migration, in VRFB diffusion is the main phenomenon to take into consideration, because the flow rate is much faster than that caused by an electric field or concentration difference, and migration is not significant in the presence of high ionic concentrations.

Ohmic overpotential

The ohmic drop is due to the electrical resistance of the materials, a measure of the ability of an object to impede the flow of charges, electrons and/or ions. It is present in the electrodes, current collectors and wires as ohmic losses, whereas in the electrolyte and membrane the resistance is towards the ions carrying charge, so we call it ionic overpotential. These two types of losses are usually referred to as the iR drop.

In general, the resistance can be found from an expression derived from Ohm's Law:

$$\eta_{ohm} = R_{ohm}I \quad (2.3.13)$$

where η_{ohm} stands for the ohmic overpotential and R_{ohm} stands for the ohmic resistance, considering both electrical resistance observed in conducting materials and ion conduction resistance in solution.

2.4 Performance indicators

Batteries can be evaluated in terms of their performance based on several parameters like their capacity, efficiency, energy density and others. These properties will be discussed in this section.

Capacity

The total **capacity** of a cell stands for the total amount of charge that can be supplied to the external circuit [47]. The capacity depends on the amount of electrochemically active species available and the number of electrons being transferred for every mole of reagent converted. The theoretical capacity of the cell can be given by:

$$Q_T = xFN_M \quad (2.4.1)$$

where x stands for the number of moles of electrons transferred during the conversion of one mole of reagent and N_M stands for the number of moles of limiting reagent. If the electrolytes are balanced and have the same number of moles, N_M for a VRFB can be found multiplying the concentration of vanadium inside the electrolyte by its total volume. This shows how the capacity of the VRFB is directly proportional to the volume and concentration of electrolyte, which is stored externally to the cell and can be easily scaled up [50].

In practice, the actual capacity is always different from Equation (2.4.1) due to different phenomena that will "consume" the reactants without contributing to the generation of current, like side reactions and crossing-over of ions. The battery's actual capacity is the number of coulombs or ampere hours delivered [47] and can be computed by:

$$Q_P = \int_0^t i dt \quad (2.4.2)$$

where i stands for the current flow for a period of time t . The ratio between the actual and theoretical capacities results on the **electrolyte utilization** factor:

$$\frac{Q_P}{Q_T} \quad (2.4.3)$$

It should be noted that the total time for the charge/discharge process to be concluded is not just the time it takes for the entire volume of electrolyte to flow through the cell, which could easily be computed knowing the flow rate. In practice, the electrolyte may be only partly consumed in one passage (depending on the flow rate, the current density and many other phenomena) so the time to fully charge the cell will be more extended.

Self-discharge is a phenomenon in which capacity is lost even when the battery is not under load. In a VRFB, self-discharge considers two different conditions, as opposed to other technologies. If the electrolyte is being pumped but there is no current flowing, self discharge considers not only the typical vanadium cross-over through the membrane but also the consumption of energy through auxiliary devices such as pumps. When the cell is in stand-by, self-discharge accounts mainly for crossing-over, which only occurs within the cell and not inside the tanks [50].

Efficiency

For rechargeable systems such as VRFB, the ability of a cell to accept charge or be recharged is measured in terms of its cycle energy efficiency. The battery's energy efficiency (EE) is simply the ratio of its energy output while discharging to the energy input while charging.

$$\eta = \frac{E_{output}}{E_{input}} \quad (2.4.4)$$

Other efficiency metrics are used when determining the cycle performance of VRFB, like the coulombic efficiency (CE), which can also be referred as the current efficiency and is defined as [47]:

$$\frac{\int_0^t i_{dis} dt}{\int_0^t i_{ch} dt} \quad (2.4.5)$$

Energy Density

The energy density is the ratio of the amount of stored energy to the battery's volume or mass, with units of kWh/kg or kWh/L. It is an important parameter because it will determine which applications are more suitable for the battery. A battery with small energy density would be preferred in stationary applications, as opposed to electric vehicles for example in which the extra weight of the batteries can represent a handicap to the car's performance.

The total available energy present in the system in Wh, E_{total} , depends on the average cell potential $U_{cell,av}$, in V, and the total capacity Q_P in Ah, as follows:

$$E_{total} = U_{cell,av} Q_P \quad (2.4.6)$$

The energy density can then be computed dividing the total energy by the total mass of the battery, m_{total} :

$$\frac{E_{total}}{m_{total}} \quad (2.4.7)$$

On the other hand, in VRFB, it makes sense to define the energy density in terms of the volume of electrolyte, $V_{electrolyte}$. The energy density of a VRFB cell then becomes:

$$\frac{E_{total}}{V_{electrolyte}} \quad (2.4.8)$$

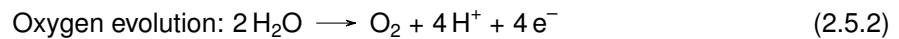
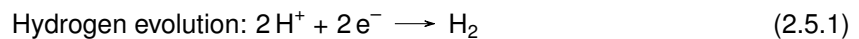
2.5 Non-ideal behaviour of VRFB

We are in the presence of an imbalanced electrolyte when the amount of active species inside one reservoir is not the same as the other. With an imbalanced system, only the half-cell corresponding to the electrolyte with the limiting active species can reach 100% SOC. In this case, the cell's SOC is not the same as each individual half-cell. This leads to a capacity and efficiency loss in the cell.

As much as we can try to produce balanced electrolytes in which the relationship between oxidizing and reducing agents is the same in both anolyte and catholyte, in practice this balance is very hard to achieve. Cross-contamination and side-reactions are the major reasons why the balance can be corrupted during long-term operations [51].

Gassing side reactions

Apart from the normal and desirable reactions occurring in a VRFB, the hydrogen evolution reaction (HER), seen in Equation (2.5.1) and the oxygen evolution reaction (OER), seen in Equation (2.5.3) could also take place, if the polarization applied to each electrode is high enough. The standard potential for HER is 0.0 V and the standard potential for OER is 1.229 V. HER takes place in the negative electrode and OER takes place in the positive electrode.



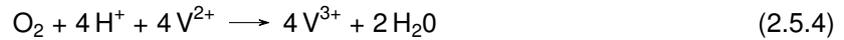
The formation of gas bubbles will result in a decrease of active surface area between the electrodes and the electrolyte, which in turn will increase the activation overpotential, so the battery will perform poorly. Mass and charge transfer are also compromised because the bubbles interfere with the proper flow distribution of the electrolyte in the porous electrode, also compromising the concentration overpotential. Gassing will also result in a lower CE because the current is not all being used for the intended reactions but also for side reactions, increasing the time required to charge the battery [51].

Another side reaction occurs in the positive electrolyte: the carbon dioxide evolution. Studies have shown that carbon dioxide evolution occurs at a potential higher than 1.6 V, causing intergranular corrosion of the graphite electrode when the polarization potential reaches 1.75 V. The standard potential for corrosion of carbon is 0.207 V which is below the standard electrode potential for anodic half reaction of VRFB, but slow kinetics allows the use of graphite in VRFB application, only becoming a problem when high potentials are applied [52]. While charging the cell, it is therefore important to set a voltage limit so to avoid that the potential at the positive electrode reaches these values.



Self-discharge side reactions

Side reactions can also occur involving V^{2+} ions which are oxidised when in contact with air [53].



Consumption of V^{2+} ions without an equivalent consumption of V^{5+} on the other half-cell will ultimately lead to electrolyte imbalance. Because of this, it is of utmost importance that the anolyte is not in contact with air at any point in time. Since this is not always possible, it is important to opt for a high ratio of electrolyte volume to electrolyte-air interface area, that is, choose a tank that leaves a small interface between the liquid and air [54].

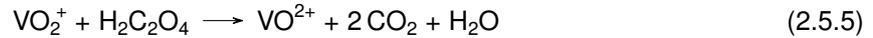
Vanadium cross-over and volumetric transfer

As mentioned before, the membrane used in VRFB has the main role of preventing short circuit between electrodes and allowing the transfer of protons and sulphate ions so that the charge balance between the half-cells can be achieved. While there has to be transfer of these species and the resistivity of the membrane should not be too high as it would increase the ohmic overpotential of the cell, the membrane should also present low permeability to vanadium ions, so to prevent the crossover of active species from one half-cell to the other. In practice, however, some cross-over tends to occur, which can lead to electrolyte imbalance. The imbalance takes place not only because of mixing of species, but also because the intruders can react with the other species and cause side reactions that lead to self-discharge [53].

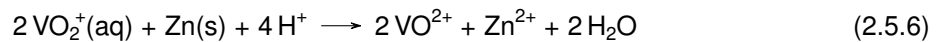
Just as ions can move through the membrane, water molecules can do the same. With water transfer, a change in concentration can occur, leading to precipitation of vanadium salts. The water transfers from low osmotic pressure to high osmotic pressure side. Furthermore, ions in solution carry water as hydration shells, and in consequence water molecules will be transferred through the membrane in the direction of these ions' movement. [55].

Different approaches can be taken in order to reestablish the balance of electrolytes after long-term operation and they depend on the cause of imbalance. Imbalance due to cross-over is often fixed through remixing of electrolytes [51]. Imbalance due to side-reactions or hydrogen/oxygen evolution is usually fixed using some sort of chemical re-balance. Chemical re-balance consists of using reducing agents such as oxalic acid, methanol, and ethanol to reduce V^{5+} to V^{4+} , compensating for the excessive

V²⁺ oxidation by oxygen [56]. The reaction with oxalic acid is as follows:



Adding organic solvents will, however, affect the electrolyte's concentration and volume balance [51]. Adding reducing metals such as Zinc to the negative electrode can also help the rebalance. The reduction goes as follows:



A novel method was proposed in which the reduction of VO₂⁺ is performed feeding hydrogen from the HER to the positive half-cell, allowing Equation (2.5.7) to occur:



It should be mentioned that re-balancing methods restore the initial capacity only partially and after they are performed the capacity tends to decrease again faster than it did before, showing that no method is still better than replacing the electrolyte altogether.

Leakage issues

Regardless of the progresses made in optimizing VRFB's architecture, some technical challenges still exist which can compromise the cell's performance. Electrolyte leakage remains as one of the main issues and it can happen internally or externally, causing efficiency loss in the cell or offering damage to other components due to the very acidic nature of the solution [57].

Leakage problems are usually avoided using sealing gaskets between the frame of the cell and the graphite plates and membrane, as this is where most of the leakage paths are. Compressing forces while assembling the cell are also a key factor to make sure that the gaskets serve their purpose. The problem arises when, even after testing, electrolyte leakage occurs only during long-term operation. While a good amount of force should be evenly supplied to guarantee full sealing, extra large stresses on particular areas of the components may lead to cracks and deformation, which will have the opposite result. Moreover, non-uniform stress distribution on the stack alone contributes for electrolyte leakage even without any damaged components [58]. Very few studies have been made in order to understand how these mechanical issues affect the cell's performance.

3

Electrochemical Techniques

As energy storage systems evolve and different materials and reagents are tested and used in their design, the strive to increase the efficiency of these systems never stops. To reach this goal, it is important to understand the mechanisms underlying the system's behavior very well. The system's electrical response can significantly help us understand the physical and chemical processes inside an electrochemical cell.

In electrochemical characterization, the potential, current and charge are the basic electrochemical properties that act as analytical signals. An electrochemical workstation is used to perform different tests and techniques in which the potential can be controlled to measure the current and vice-versa. Such techniques can be cyclic voltammetry (CV), galvanostatic charge-discharge (GCD) and electrochemical impedance spectroscopy (EIS).

Electrochemical characterizations can be performed on two electrode systems, which was the arrangement used in this work. In this case, we have the positive electrode as the working electrode and the negative electrode as the counter electrode. With this setup, the open circuit potential is the potential difference across the cell

3.1 Polarization curves

Measuring the cell voltage against several values of current allows the study of what is called the polarization curve of said cell. These curves are often called performance curves as well, as they enable us to take several conclusions about the characteristic behavior of the cell.

It was shown how the flow of current is inherently correlated with an overpotential, which can be related with different electrochemical mechanisms undergoing inside the cell. However, there are certain points in which specific phenomena get dominant over others. Typical polarization curves for electrochemical cells usually show three different regions, as it can be seen in Figure 3.1.

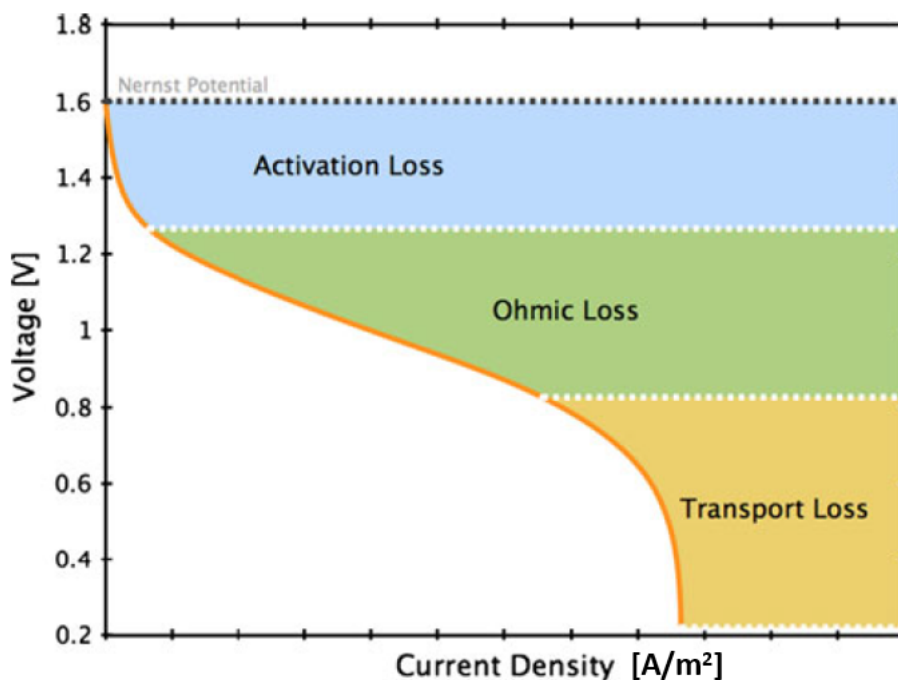


Figure 3.1: Generalized polarization curve for a VRB indicating the dominant source of overpotential in each region [3].

In the first region, for low current density, an intense voltage drop is seen, due to the activation overpotential. The second region is almost linear, consisting in ohmic losses, and it is associated with the internal resistance of the cell, which includes the ionic resistance of the electrolyte, the ionic resistance of the membrane and the mass-transfer of redox-active species within active electrode areas. The third and final region stands for the transport losses [47]. As the voltage decreases, the current is unable to keep a linear evolution, and we see it decays to a limiting current.

Polarization curves can be performed in a galvanostatic way, in which the current is controlled and the potential varies accordingly, or in a potentiostatic way, in which the potential is controlled and the current is measured [3].

Different parameters need to be set for the potential linear sweep that results in a polarization curve. The scan rate is the speed of voltage variation [59], in mV/s. The E step defines the potential difference between each point of the measurement, which gives the resolution of the measurement [60]. For example, an E step of 5 mV and a scan rate of 20 mV/s will have the potentiostat take one second to measure the first 4 points of the curve, so it has a specific time available for each measurement. Low scan rates are often preferred as they give the current the needed time to stabilize for each voltage being applied.

3.2 Electrochemical Impedance Spectroscopy

In Impedance Spectroscopy, the linear electrical response of the system is analyzed to yield useful information about its physicochemical properties. One of the advantages of this technique is that it can be performed several times without altering the electrochemical properties of the system. It can be done in potentiostatic or galvanostatic conditions. In potentiostatic conditions, a small sinusoidal voltage perturbation (5 to 20 mV) of known amplitude and frequency is applied, creating a current response, also sinusoidal, and the impedance of the system is the relationship between them, taking into account both phase shift and amplitude of the signals [22, 61]. Using an expression homologous to the Ohm's Law, the impedance of the system is given by:

$$Z(\omega) = \frac{E}{I} = |Z| \cos \Phi + |Z| \sin \Phi j \quad (3.2.1)$$

where Z stands for the system's impedance, E stands for the potential, I stands for the current applied, ω stands for the angular frequency of the signal and Φ stands for the phase angle shift between the potential and current signals.

In electrochemical systems, the current density, in Ampere/cm², is often used, and the impedance is inversely proportional to the active area:

$$\eta = Zi \tag{3.2.2}$$

where η is the system's overpotential in Volts and i is the current density in Ampere per unit of area, which makes the units of Z Ohm units of area.

In Equation (3.2.1) it can be seen how the impedance is composed of both a real part and an imaginary part, which means it is composed by resistive and reactive components. To analyze EIS spectra, Nyquist plots as seen in Figure 3.2 are often used. The symmetric of the imaginary part is usually presented, as it tends to be negative in electrochemical systems. The impedance can be represented as a vector (arrow) of length $|Z|$. The angle between this vector and the horizontal axis is the phase angle shift. Each point of the plot corresponds to a different frequency. In a Nyquist plot the frequency of each point is not explicit, however the plot starts at high frequencies and ends at the lowest frequencies [62].

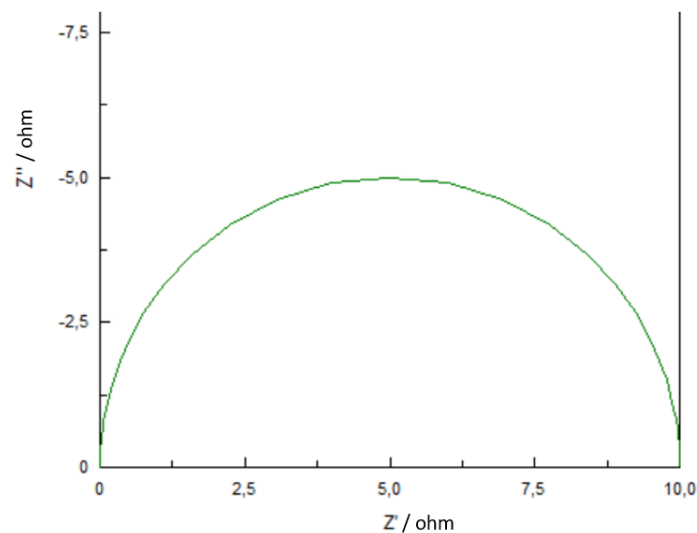


Figure 3.2: Example of a Nyquist Plot for a simple RC parallel circuit. $R=10 \Omega$; $C=0.005 \text{ F}$.

Another popular representation method is the Bode plot, which can be seen in Figure 3.3. The impedance is plotted with the logarithm of the frequency on the horizontal axis and the absolute value of the impedance ($|Z|$) or the phase-shift on the vertical.

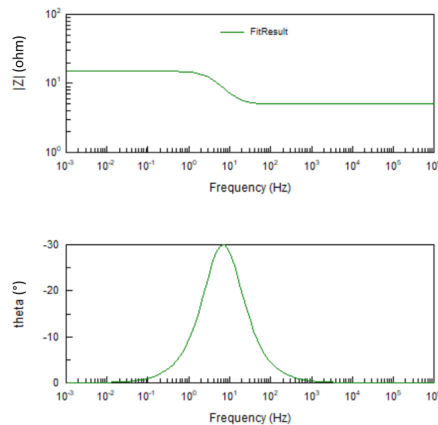


Figure 3.3: Example of a Bode plot for simple RC parallel circuit. $R=10 \Omega$; $C=0.005 \text{ F}$.

A common way to interpret EIS spectra is correlating it to an equivalent electric circuit model, composed by simple elements such as resistors, capacitors and inductors, that will accurately represent the physical processes occurring in the electrochemical cell. Using an equivalent circuit previously predicted for that specific system, a fitting to the experimental results is performed to get values of impedance for each element. Another approach would be to take the physical equations that describe each process and calculate the respective impedance, which can become much more complicated.

The system must be kept at a steady state throughout the time required to take the EIS measurements, which depends on the frequency range. For a frequency range from 100000 Hz to 0.01 Hz, it may take around 10 minutes to do one measurement. The signal must be small enough that we can assume a linear system [63].

EIS spectra for electrochemical cells

Electrochemical cells are usually represented by an equivalent circuit consisting of a resistor in series with two resistor-capacitor parallel networks, as seen in Figure 3.4. Each circuit element represents a different physical phenomenon occurring inside the cell. R_S , the series resistance, stands for the ohmic drop inside the cell and is the interception of the graph with the horizontal axis at high frequencies. Two capacitive loops then follow, represented by two resistor-capacitor parallel networks in the circuit model. The first loop is often attributed to charge-transfer effects, its diameter R_1 accounting for the charge-transfer resistance and the capacitor representing the double-layer formed at the electrodes' interface. At low frequencies the transport effects are represented. Different studies conducted by Leuaa et al [64, 65] found that mass transport effects can have different behaviors: a finite behavior, with the shape

of a semi-circle, where internal transport, that is, the vanadium ion transport through the porous medium of the electrode, is dominant; or a semi-infinite linear behavior, represented by a Warburg element in the electric circuit, when the external diffusion of ions from the bulk of the solution to the porous electrodes is the dominant mass transport process. Predominance of one process over the other dictates the shape of the spectra, and sometimes a mixture of the two can be observed.

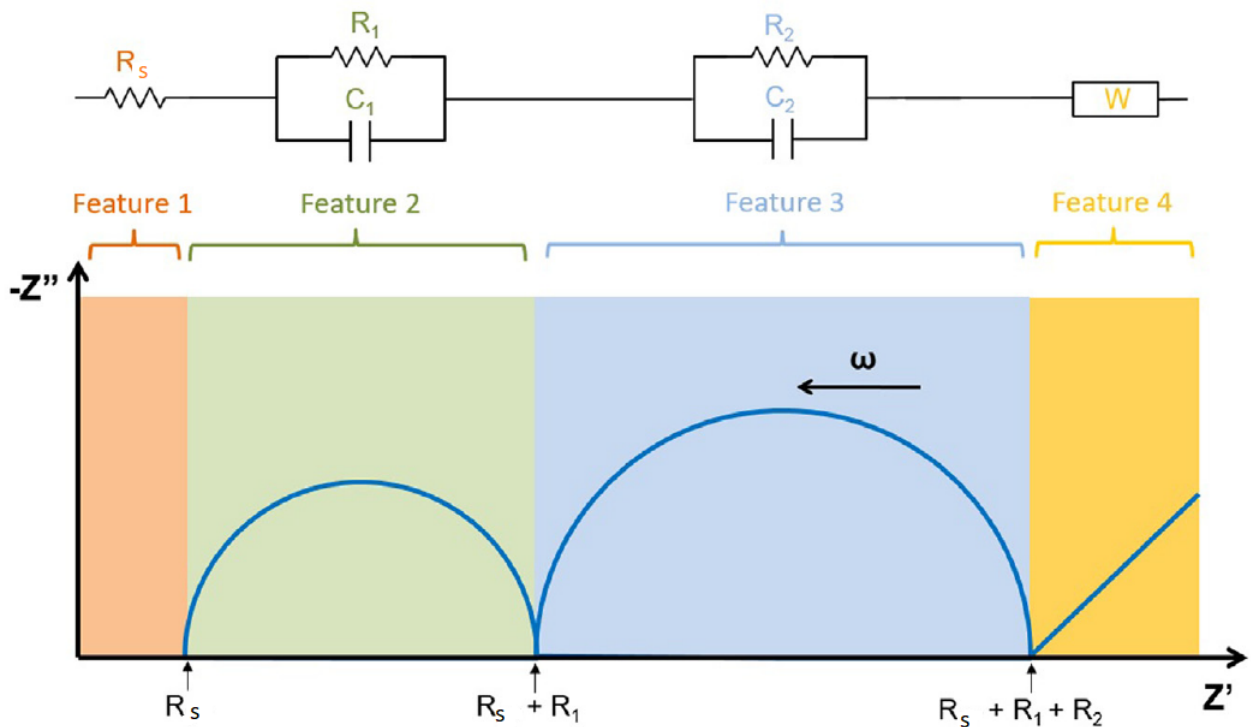


Figure 3.4: Schematic idealized impedance complex plane plot for a VRFB cell [4]

Experimental EIS spectra rarely show perfect semicircles like the ones seen in Figure 3.4, which suggests a non-ideal behavior of the capacitors. Depressed semicircles can be explained by different phenomena, depending on the type of system. Sometimes they are explained by surface heterogeneity or roughness [66]. For this reason, Constant Phase Elements (CPE) are usually added instead of ideal capacitors. The impedance of a CPE can be seen in the following equation:

$$Z_{CPE} = \frac{1}{(j\omega)^{\alpha Q}} \quad (3.2.3)$$

where α stands for an exponent that varies ranging from 0 to 1. When α equals 1, the CPE behaves like

an ideal capacitor, and Q is its capacitance.

One cannot assume that an equivalent circuit that produces a good fit to a set of data represents an accurate physical model of the cell. Adding enough elements to the circuit one can fit nearly any impedance spectrum, but can be left with a circuit that has no representation of the real system. One way to verify the model is to alter a single cell component and see if you get the expected changes, experimentally. Making sure the model has a real representation of the cell is the most important aspect when reflecting on the validity of the results. Another way to validate the results is by considering the error for each element in the fitting given by the software and checking if it is smaller than the actual value for that component. Lastly, the goodness-of-fit parameter, χ^2 should be checked. The closer it is to zero, the better the results fit the experimental data [67].

4

Experimental Conditions

4.1 Electrolyte

Two concentrations of vanadium were used in the experiments, 1.25 M and 0.121 M, and a sulfuric acid concentration of 5 M. The solutions were prepared by dissolution of vanadium pentoxide.

To prepare the 1.21 M electrolyte, vanadium pentoxide was first dissolved in sulfuric acid until solution of 1.25 M vanadium and 5 M sulfuric acid was achieved. This solution had been previously prepared, so it was already available at the laboratory. From this solution, in which all vanadium species are in the V^{5+} state, 400 mL were taken. Before feeding the electrolyte to the cell, it was necessary to reach a $V^{3.5+}$ solution. The first step was to convert all VO_2^+ species to VO^{2+} , for which 31.52 g of oxalic acid were added. The standard reduction potential for oxalic acid is - 0.49 V against 1.00 V for the reduction

of V^{5+} , which makes the reaction spontaneous. At room temperature, the reaction should reach 90-95% conversion in 6-8 hours [25], so it was left overnight with stirring. The next day, the solution had turned from yellow to blue, showing that VO_2^+ had successfully been converted into VO^{2+} . Further reduction of the vanadium species will not be as spontaneous, the standard potential of reduction for the VO^{2+}/V^{3+} couple being 0.337 V. Because of this, zinc, with a standard reduction potential of -0.76 V, was used as a reducing agent to achieve a mixture with 50% VO^{2+} and 50% V^{3+} . A secondary reaction occurs when adding Zinc to produce hydrogen as follows:



Some excess of Zn was therefore added to the mixture, to compensate for the secondary reaction, and 10 g (0.153 moles) were added. Both reactions with oxalic acid and zinc present water as a byproduct. For this reason, the volume of solution was measured once again after both reactions. With a volume of 414 mL, the solution was left with a vanadium concentration of 1.21 M.

The $V^{3.5+}$ solution was then divided in two different tanks and fed to the flow cell. An OCP of 0 V was observed, as expected, since both electrolyte tanks contain the exact same solution. Applying a current flow led to a V^{3+} solution in the negative electrode and a V^{5+} solution in the positive electrode. This represents a VRFB ON 0% SOC, and the cell is ready to use. The 0.125 M electrolyte had been prepared and used in previous works so no preparation was needed.

4.2 Cell Assembly

The VRFB used in this work was previously developed by another student doing his internship at the Laboratory of Corrosion Science and Surface Engineering of Instituto Superior Técnico. It was based on the architecture of commercial cells, although a reduction in cost was attempted. The outer structure of the cell consists of two PTFE plates with 20 mm thickness. This material presents some favourable characteristics such as low cost, high mechanical rigidity and chemical stability. It is also a non-conductant material. Two alignment rods are used to help assemble the system in place. Each half-cell consists of one **current collector** made of copper, a graphite plate and a PTFE frame with carbon felts inside.

The **graphite plate** electrodes were Sigracell PV15 graphite supplied by SGL Carbon (Germany), consisting of 15% of Fluoropolymer in addition to graphite. The **PTFE frame** had external dimensions of 100x100 mm with 20 mm thickness and an inner cut of 50x50 mm to accommodate 3.5 **carbon felts** of

the type SGL Carbon Sigracell GFA 6 EA. Each felt has a thickness of 6 mm and a porosity of 95%. On each side of each one of the PTFE frames a **silicone gasket** with 1 mm thickness cut into the shape of the PTFE frame including two holes for the alignment rods was placed to help sealing the cell and avoid any leakage. The gaskets help sealing against the graphite plate electrodes on one side and against the membrane on the other. Between the two half-cells a **Dupont Nafion 117 membrane** was placed. The schematic for the cell assembly is shown in Figure 4.1.

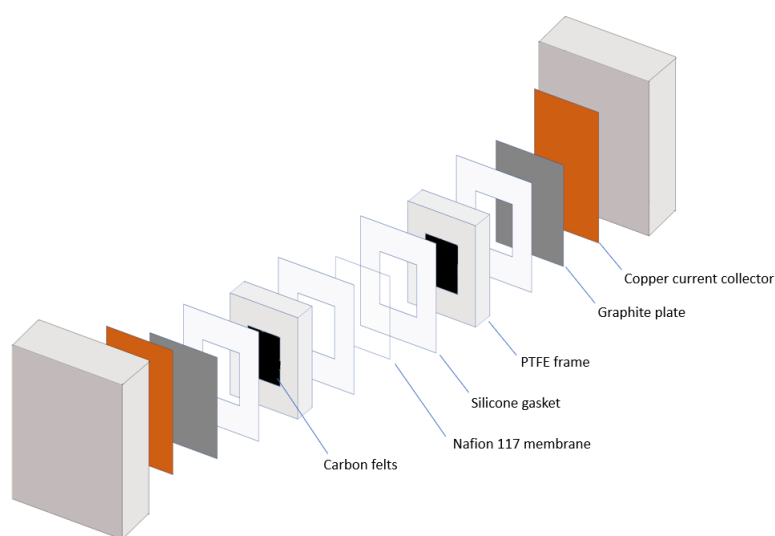


Figure 4.1: Schematic of the assembly of the cell.

Before it was ready to use, the membrane was activated. This process consisted on boiling the membrane in 3% w/v hydrogen peroxide for an hour in order to remove all the impurities, then boiling it in distilled water for one hour, followed by slightly boiling it in sulfuric acid 3 M for one hour at 80 C in order to increase the amount of protonated sulfonic acid groups to enhance the overall ionic exchange ability of the membrane and finally boiling it in water again for another hour [68].

The final assembly of the cell is done by tightening the screws. To ensure good sealing, enough force should be applied to see slight compression of the silicone gaskets, without however, causing permanent damage. The full cell can be seen in Figure 4.2.



Figure 4.2: Fully assembled VRFB cell.

Small containers were used to store the electrolyte, with the goal of reducing the contact between the solution and air, to avoid secondary reactions mentioned in Chapter 2. As the piping system, Teflon pipes with 6 mm external diameter and 4 mm internal diameter were used, as well as silicone ones to work with a GILSON™ Minipuls 3 peristaltic pump, which reaches a maximum flow rate of 48 rpm or 21.8 mL/min (calibration curve made with water). The final setup can be seen in Figure 4.3. The plastic container is used as a safety measure in case leakage occurs.

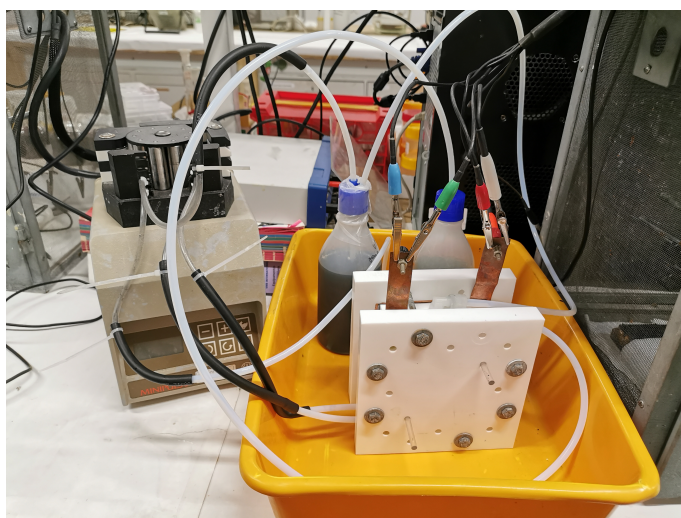


Figure 4.3: VRFB set-up for experimental measurements.

4.3 Testing conditions

All measurements were made using a Gamry 5000 Potentiostat. The values of current density and impedance are normalized for an active area of 25 cm^2 . The fittings to all the experimental data from EIS were performed using the ZView software.

Charge/discharge cycles

To study the charge-discharge behaviour of the cell for different current densities, 4 charge-discharge cycles were performed for the current densities of 4, 8 and 12 mA/cm^2 . The first step of the cycle to be performed was the charging step. The cycles were performed with no electrolyte circulation.

Polarization curves

Polarization curves were taken for both concentrations of electrolytes, 0.125 M and 1.21 M. The cell was charged with a current of 0.1 A to a voltage limit of 1.8 V to avoid overcharging. The discharging polarization curves were then performed with a scan rate of 0.002 A/s, starting at 0 A and stopping when the potential hits 0 V.

Electrochemical Impedance Spectroscopy

All EIS measurements were made under the following testing conditions:

- Frequency range: 100000 Hz to 0.03 Hz;
- AC Voltage: 5 mV;
- Points per decade: 8.

For EIS measurements it is important that the system is stable, therefore the OCP was measured for 10 minutes before all measurements to ensure that there was not a change in potential higher than 10 mV.

State of charge

Different levels of charge were tested for a vanadium concentration of 0.125 M. The cell was charged

at 0.1 A with a voltage limit of 1.8 V, reaching 86% SOC, and EIS measurements were made. The cell was then discharged for around 5 minutes under a 0.1 A current, OCP was measured and EIS was performed. Measurements were made under a flow rate of 20.4 mL/min until a SOC of 0%, that is, 800 mV OCP, was achieved. Measurements at a SOC higher than 86% were attempted, surpassing the voltage limit when charging, but corrosion at the positive electrode occurred due to overcharge and those EIS results were inconclusive in regards to the SOC influence.

Because EIS results are usually difficult to reproduce, another set of experiments was performed in which no circulation was ever present. Discharge was performed with a current of 0.1 for only 2 minutes. After reaching 0% SOC, the cell was charged to its maximum once again and the experiments were repeated, to see if the results were consistent, and they were.

Number of membranes

To study the effect of the number of membranes in the EIS spectra, 0.125 M electrolyte was used. The cell was charged until it reached an OCP of 1.45 V, which is quite stable and that way no extra charging/discharging was needed throughout the entire experiment. Three Dupont Nafion 117 membranes were tested individually, in combinations of two and finally in a combination of the three.

Number of felts

To study the effect of the number of membranes in the EIS spectra, the 1.21 M electrolyte was used. The cell was charged until it reached a SOC of 1.56 V so that no charging/discharging was needed throughout the entire experiment, because without the felts it impossible to charge/discharge the cell. At this electrolyte concentration the cell was able to hold a stable potential even at such high level of SOC. EIS measurements were taken with 3.5 felts in each half-cell as normal and afterwards they were removed from both half-cells and EIS measurements were made again.

5

Results and Interpretation

5.1 Charge-discharge cycles

To study the charge/discharge behavior of the cell, charge/discharge cycles at constant current densities were performed. For each applied current density, 4 cycles presented the exact same curves, overlapping with each other. The similarity shows that there is no capacity loss from one cycle to the other.

The curves for the different current densities are shown in Figure 5.1. First, a small increase in potential is observed, represents the overpotential being applied to charge the cell. The process then follows a linear progression, until around 1.6 V, at which point the potential suddenly increases, meaning that the charge process is over and other reactions will start to take place. The discharge process then begins,

with a sudden potential decrease (negative overpotential). The discharge process also follows a linear progression, until the entire electrolyte is discharged and the potential falls abruptly. It can be seen that for a higher current density the time it takes to completely charge and discharge decreases accordingly.

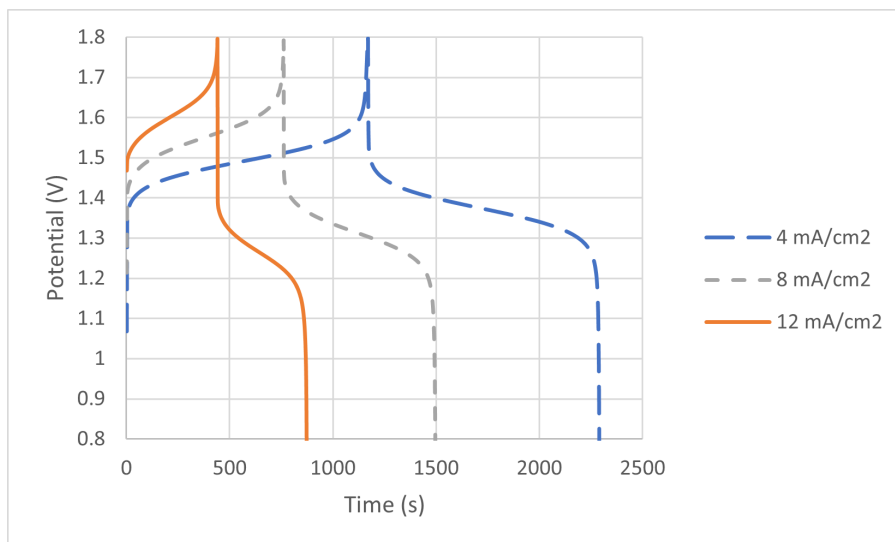


Figure 5.1: Charge-discharge curves for the current densities of 4, 8 and 12 mA/cm², with stagnant electrolyte at a concentration of 0.125 M.

Using Equation (2.4.5) and the results obtained from Figure 5.1, the cell's coulombic efficiency was computed. Because the current is constant in both charge and discharge processes, the time of discharge/time of charge ratio gives the CE of the cell. The results for CE and the total charge applied for each current density can be seen in Table 5.1.

Table 5.1: Total charge and Coulombic Efficiency for the different current densities.

Current Density (mA/cm²)	4	8	12
Total Charge (mAh)	33	42	37
Discharge Eff. (%)	96	98	98

The total charge applied in each experiment should be the same, but deviations of 12% to 30% were observed between them. The electrolyte being stagnant during all the tests, it could be possible that some mass transport issues occur, and in some of the measurement not all of the active species present are converted. The coulombic efficiency computed from all three charge/discharge cycles is a good indicator of the battery's performance, independently of the current density used. Similar values were obtained by Wang et al [69], for a flow rate of 60 mL/min.

Formal potential

The formal potential was introduced in Chapter 2 as a way to account for the concentration of hydrogen ions, and the activity coefficients in the Nernst equation. The formal potential can be measured experimentally and it corresponds to the OCP for which the cell's SOC is 50%. The charge-discharge curves shown in Figure 5.1 were used to assess the cell's potential half-way through the process of charge/discharge, which is not the OCP because it is affected with an overpotential necessary for current to flow. The average between the two points of potential 50% SOC is the OCP, considering the same kinetics for both directions of the reactions occurring in the cell. To get a better estimate, the three charge-discharge curves can be used to get an average result that will be the most accurate for the system. The data can be found in Table 5.2 and resulted in a formal potential of 1.43 V, which was used in Equation (2.2.12) to create a plot in which the SOC can be assessed from the cell's OCP, which can be seen in Figure 5.2. The "Actual potential" for all three current densities does not present significant deviations, which shows that the result holds for different conditions of operation.

The formal potential obtained is in reasonably good agreement with other authors who used an identical procedure. Tang et al [53], with an acid concentration of 5 M like the one used in this work, measured a formal potential of 1.4 V, which is often used directly as an assumption by other authors [49]. For a vanadium concentration of 1.6 M, Haisch et al [48] achieved a formal potential of 1.35 V, but did not specify the acid concentration, which could be the reason for the deviation.

Table 5.2: Data gathered to assess the formal potential of the cell.

		100 mA	200 mA	300 mA
Charge	Total time (s)	1170	760	440
	Middle time (s)	585	380	220
	Middle potential (V)	1.493	1.569	1.604
Discharge	Total time (s)	1124	742	432
	Middle time (s)	562	371	216
	Middle potential (V)	1.373	1.311	1.260
Actual potential (V)		1.433	1.440	1.432
Formal potential (V)		1.43		

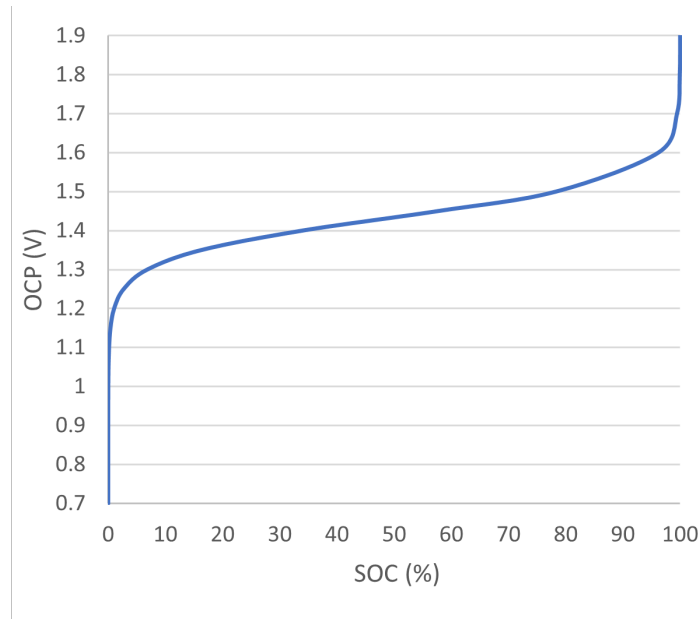


Figure 5.2: Evolution of cell potential with SOC, for a formal potential of 1.43 V, $T=298\text{K}$, calculated from Equation (2.2.11).

5.2 Polarization curves

To vary the flow rate at which the electrolyte is pumped through the cell, different speeds at the peristaltic pump were used. To assess the flow rate correspondent to each speed, a calibration curve was performed before-hand, but with water, which is not as viscous as the acidic solutions used in the experiments. However, peristaltic pumps apply the required pressure needed to maintain a certain flow rate, although within limits, so no great deviations are expected to occur.

Polarization curves are seen in Figure 5.3 and Figure 5.4. For both concentrations the region of activation polarization is not seen in the results, maybe because it is too small. For a vanadium concentration of 0.125 M, the limit current undergoes a 17% increase between flow rates of 9.4 to 20.4 mL/min. Similar results were found by Aaron et al [3] for a vanadium concentration of 1 M, although higher current densities of up to 300 mA/cm^2 are reached by Aaron et al against the 9.2 mA/cm^2 reached in this work, possibly due to the different concentrations. In this work, for a vanadium concentration of 1.21 M, no limit current is observed, but current densities as high as 90 mA/cm^2 are reached.

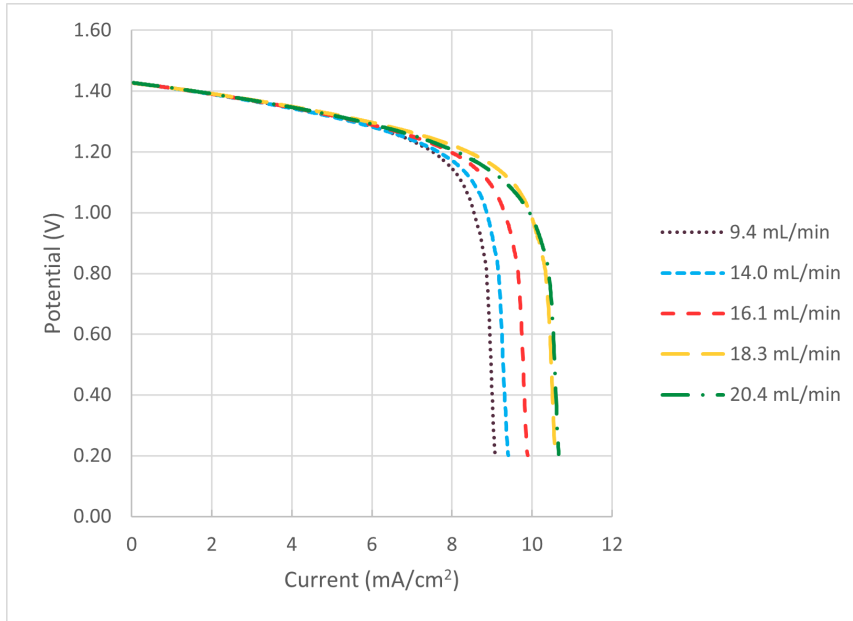


Figure 5.3: Discharging polarization curves for a concentration of 0.125 M at different flow rates, with a scan-rate of 2 mA/s.

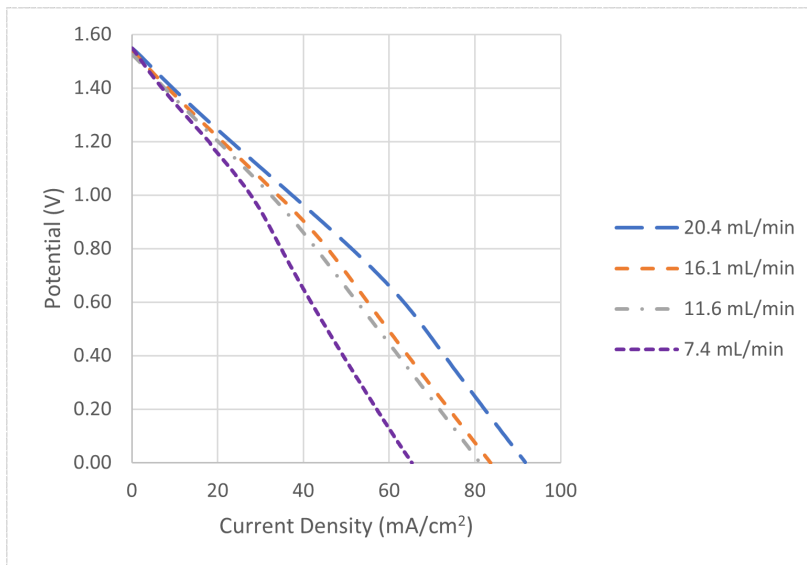


Figure 5.4: Discharging polarization curves for a concentration of 1.21 M at different flow rates, with a scan-rate of 2 mA/s.

For a concentration of 1.21 M, polarization curves show only the ohmic region, where the relationship between the potential and the current is linear, but two different slopes are observed for each one. This could be explained by a change in SOC due to continuous polarization, which is avoided when using a significantly high amount of electrolyte like the one used for the less concentrated solution, 800 mL in

each tank. For a greater concentration the volume used was only 207 mL to facilitate charge/discharge processes, and consequently the SOC during discharge polarization did not remain the same.

Figure 5.5 depicts the effect of the concentration on the discharge curves. The curve's slope at the linear region, where ohmic losses are predominant, gives the cell's ohmic resistance. In this study, for a flow rate of 16.1 mL/min and a concentration of 0.125 M and 1.21 M, the computed resistance was of $36 \text{ m}\Omega \text{ cm}^2$ and $17 \text{ m}\Omega \text{ cm}^2$, respectively. For Aaron et al [3] the resistance was $2 \text{ m}\Omega \text{ cm}^2$.

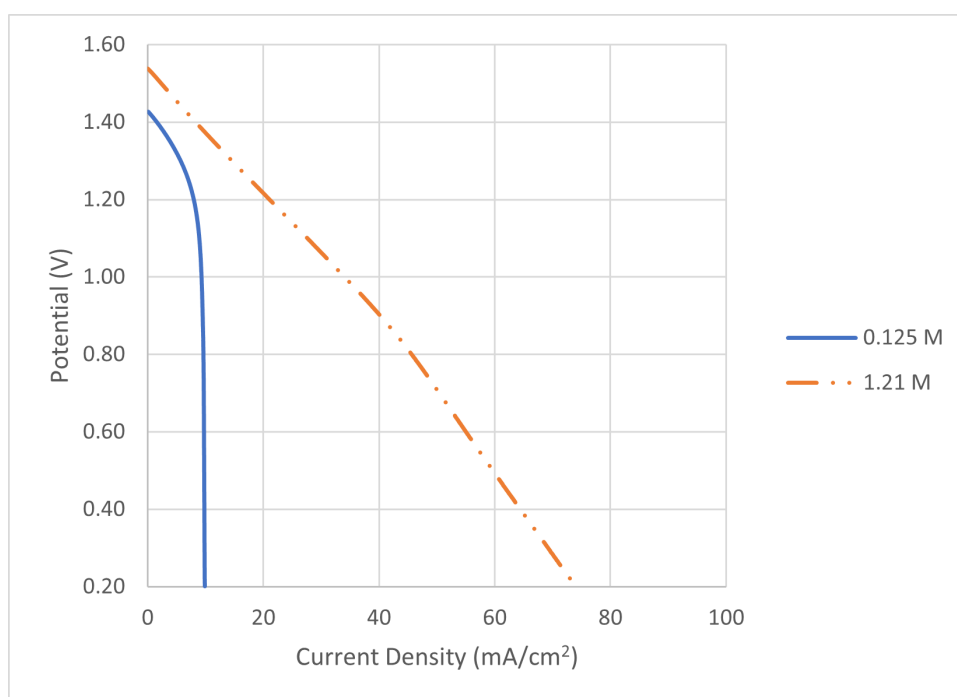


Figure 5.5: Polarization curves at a flow rate of 16.1 mL/min for different vanadium concentrations, 1.21 M and 0.125 M, with a scan-rate of 2 mA/s.

5.3 Electrochemical Impedance Spectroscopy

The main focus of the work is the characterization of the cell using impedance spectroscopy. The technique was therefore applied to the cell using a few different configurations and working conditions. A representative impedance spectrum is presented in Figure 5.6, where two capacitive loops are observed, as well as a distorted and ill-defined loop at the high frequency region. Before the interception with the horizontal axis, a tail of points with positive imaginary part represents some inductive effects which are associated to the cell's experimental set-up and electric materials [4]. For the purpose of this study, these

points were neglected. High-frequency intersection with the real axis represents the ohmic resistance of the system. Decreasing the frequency, a capacitive behavior starts to develop, creating a capacitive loop, whose diameter represents the charge-transfer resistance. When two semi-circles are observed instead of one, lower frequency one is believed to represent the mass transport effects on the impedance [70, 71, 72, 64, 65].

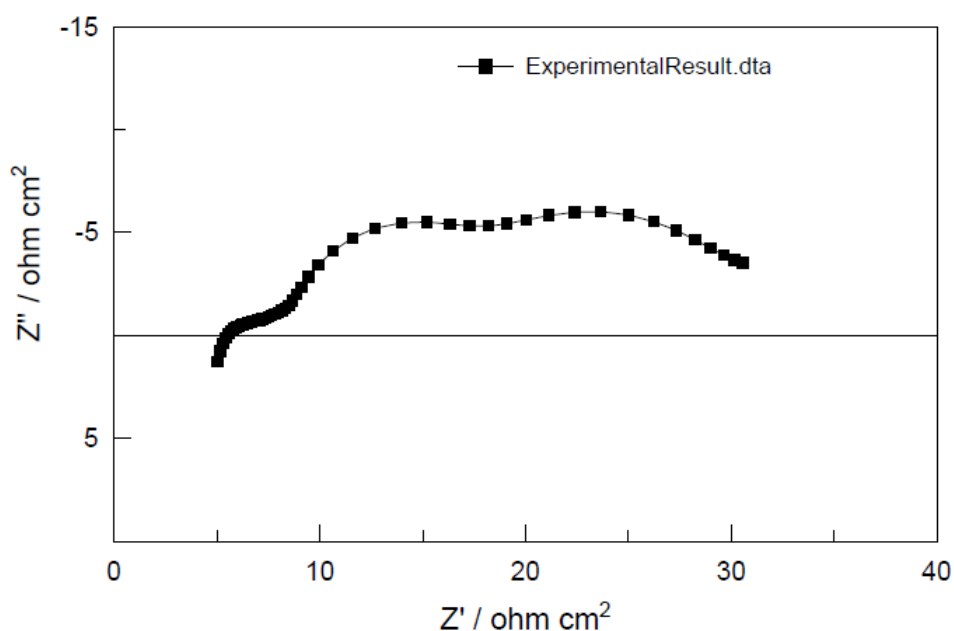


Figure 5.6: Impedance spectrum for the VRFC with a vanadium concentration of 0.125 M, electrolyte flow rate 24.1 mL/min, at the cell's spontaneous potential.

EIS experimental data was treated using ZView software. Fittings with two different circuit models were performed, as seen in Figure 5.7 and Figure 5.8. The errors of the fitting for each element are smaller when using only a CPE element instead of an RC parallel network to represent the irregularity at high frequencies, even if the first presents worse overall goodness-of-fit (χ^2). High values for the individual errors are bad indicators for the accuracy of the proposed circuit model. These results support the idea that the irregular shape seen at high frequencies is not related to charge-transfer effects. The ohmic resistance estimated for the system is therefore $3.9 \Omega \text{ cm}^2$, the charge-transfer resistance $6.1 \Omega \text{ cm}^2$ and the mass-transport resistance $7.6 \Omega \text{ cm}^2$.

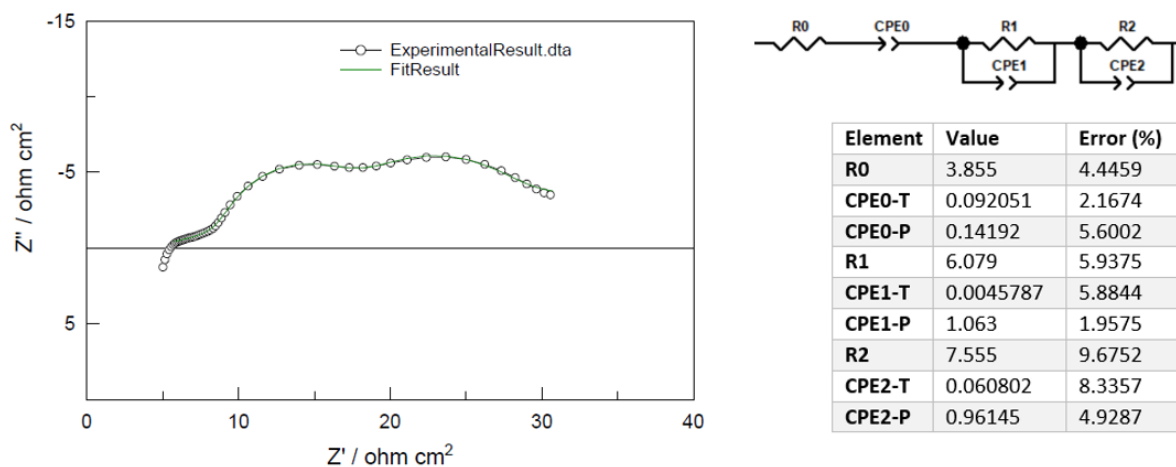


Figure 5.7: Fitting results directly taken from ZView Software for a vanadium concentration of 0.125 M, flow rate 24.1 mL/min, DC polarization 0 mV using a circuit model with 2 RC networks in series with a resistor and a CPE, where units for R are $\Omega \text{ cm}^2$, for CPE-T are $\text{F cm}^{-2}\text{s}^{\alpha-1}$, and CPE-P has no units. $\chi^2 = 9.9 \times 10^{-5}$.

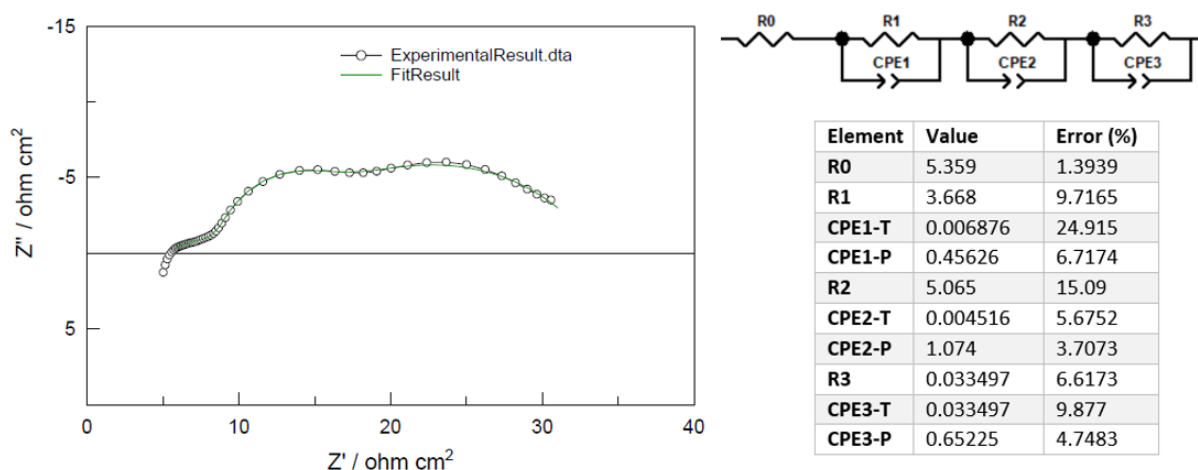


Figure 5.8: Fitting results directly taken from ZView Software for a vanadium concentration of 0.125 M, flow rate 24.1 mL/min, DC polarization 0 mV, using a circuit model with 3 RC networks in series with a resistor, where units for R are $\Omega \text{ cm}^2$, for CPE-T are $\text{F cm}^{-2}\text{s}^{\alpha-1}$, and CPE-P has no units. $\chi^2 = 6.7 \times 10^{-5}$.

In order to analyze the effect of the active area, experiments were done using the cell without the carbon felts. analyzing Figure 5.9, it can be seen that the phase angle at high frequencies remains low and steady when there are carbon felts in the cell, whereas having no carbon felts results in a regular peak which translates into a regular arch in the Nyquist plot. The irregular shape observed at high frequencies can therefore be related to the presence of the carbon felts, rather than a charge-transfer process, and it was therefore disregarded during interpretation of the results.

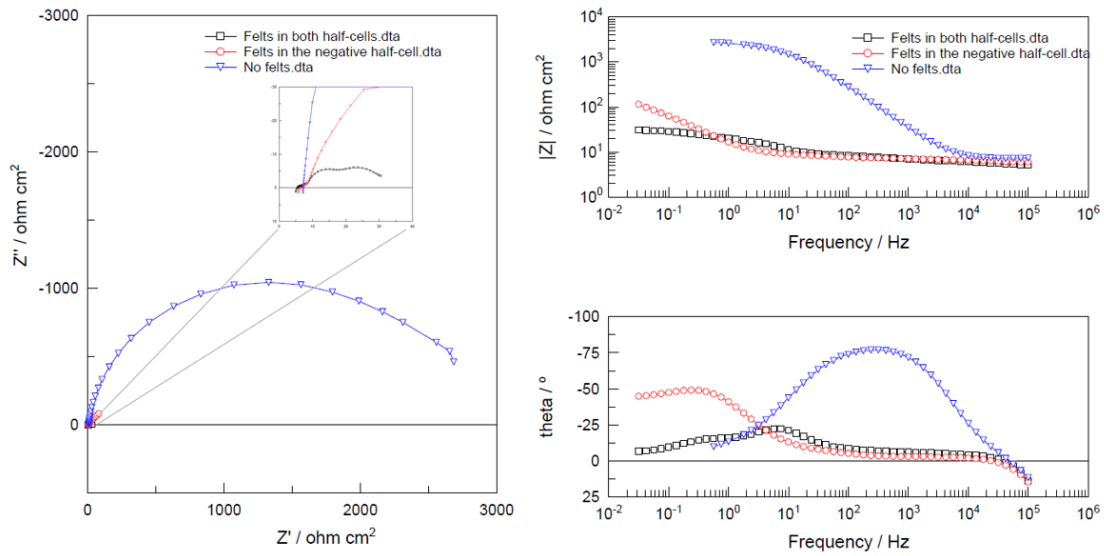


Figure 5.9: Nyquist and Bode plots obtained at a vanadium concentration of 0.125 M having carbon felts in both half-cells, only in the negative half-cell and no carbon felts at all.

Number of membranes

To test the effect of the number of membranes in the cell's resistance, EIS measurements were performed using 1, 2 and 3 Nafion membranes, and a significant increase in ohmic resistance is found (Figure 5.10). The transfer of protons through the membrane is affected by some ohmic resistance, so the change in the high frequency resistance was already expected. Changes in the faradaic resistance are most likely due to SOC differences rather than the number of membranes. Fittings were performed using the equivalent circuit as seen in Figure 5.11, where an example is presented. This time, the irregular shape at high frequencies was best fitted to a RC parallel network. High values of error for the CPE1-T element were not concerning as it was decided to disregard the irregular shape at high frequencies. The remaining residual errors for each component stayed below 16%, which supports the proposed circuit model.

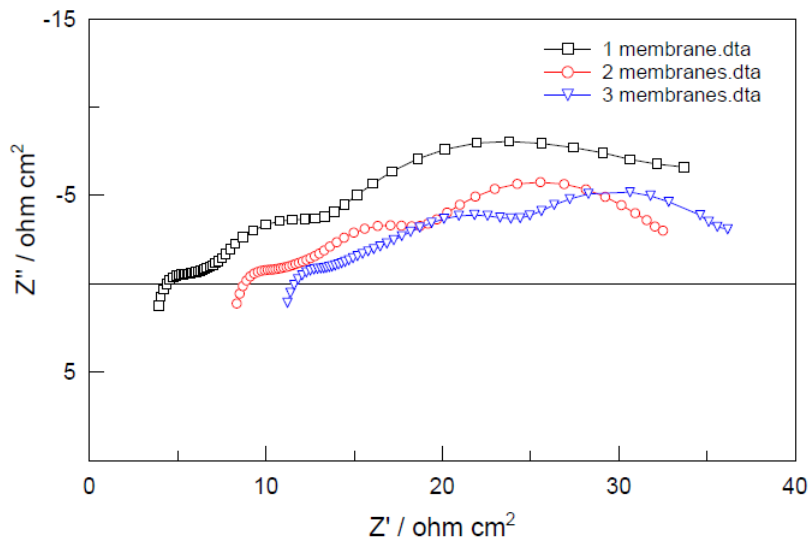


Figure 5.10: Impedance spectra of the VRFC with the setup using single or multiple Nafion membranes; flow rate 20.4 mL/min, concentration 0.125 M.

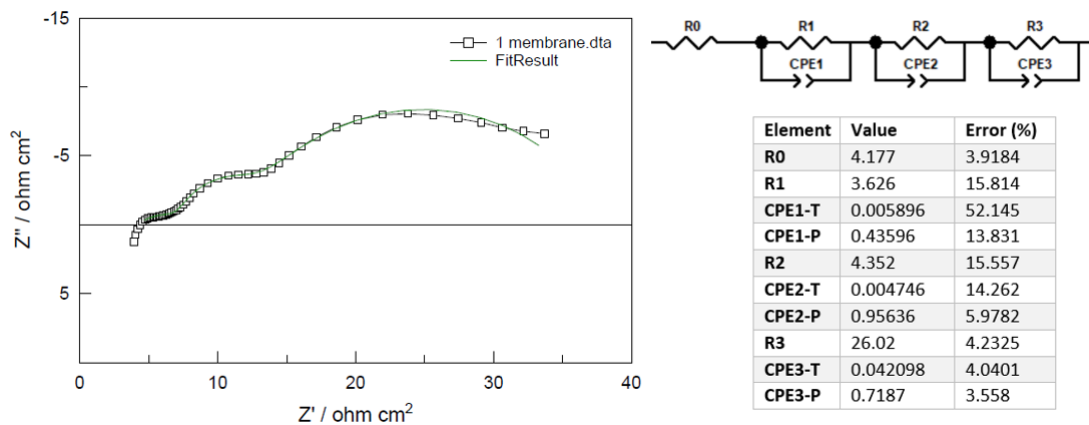


Figure 5.11: Fitting result directly taken from ZView Software for the Nyquist plot obtained for one membrane, where units for R are $\Omega \text{ cm}^2$, for CPE-T are $\text{F cm}^{-2} \text{ s}^{\alpha-1}$, and CPE-P has no units.

The evolution of R_0 with the number of membranes shows in that the ohmic resistance is directly proportional to the number of membranes - Figure 5.12. Considering the trending line, the ohmic resistance of the cell, having only one membrane, was determined to be $3.9 \Omega \text{ cm}^2$, close to the value obtained by Ghirlanda [45], $3.13 \Omega \text{ cm}^2$. Other authors got smaller values of resistance, but in the same order of magnitude. Becker et al [73] showed ohmic resistances around $1.2 \Omega \text{ cm}^2$, Li et al [49] showed values of around $1.4 \Omega \text{ cm}^2$ and Sun et al [74] showed values of around $1.1 \Omega \text{ cm}^2$.

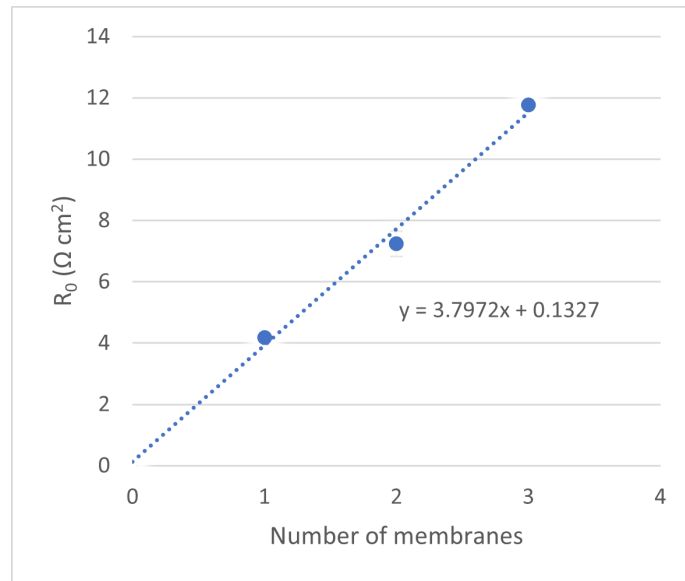


Figure 5.12: Evolution of the high frequency resistance with the number of membranes.

The trend line in Figure 5.12 was added so that the interception with the horizontal axis could be calculated. This is the value of internal resistance of the cell disregarding the membrane, that is, the resistance of all the other components (wires, current collectors, ionic resistance in the electrolyte). This resistance was found to be $0.13 \Omega \text{ cm}^2$.

Effect of the State of Charge

EIS measurements were performed at different SOC both with circulation and using fluid static conditions. Some of the spectra are seen in Figure 5.13 and Figure 5.14, where clear changes at low frequencies are observed.

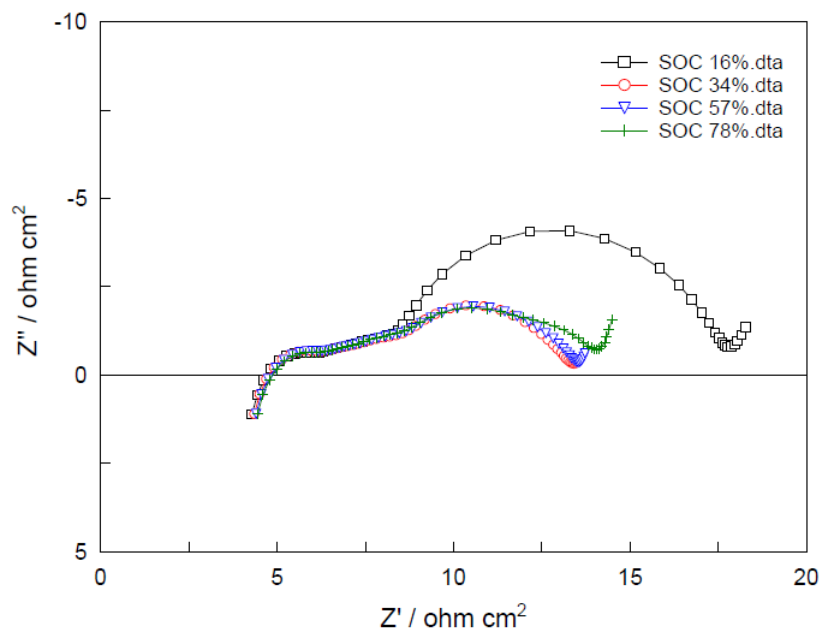


Figure 5.13: Impedance spectra of the VRFC obtained for different levels of SOC; vanadium concentration of 0.125 M and flow rate of 20.4 mL/min.

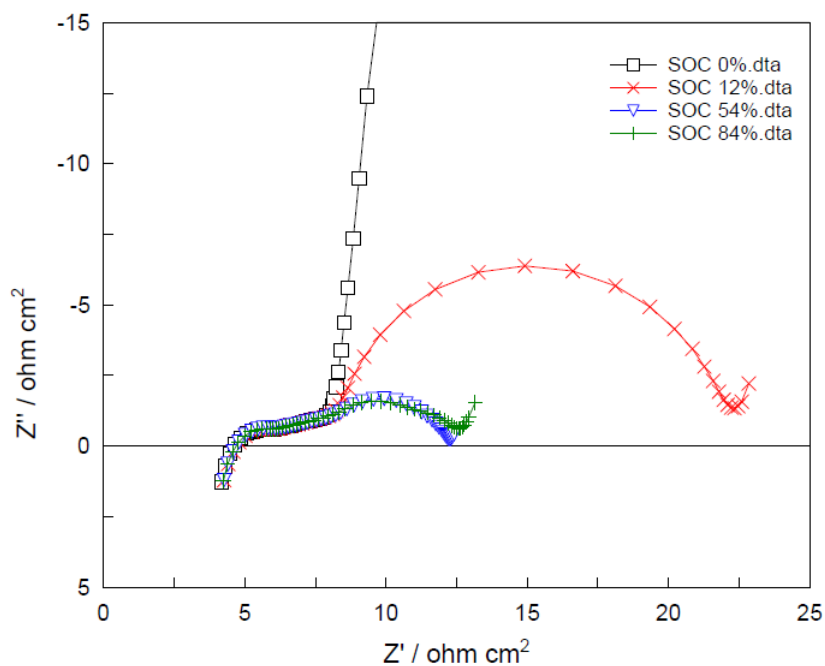


Figure 5.14: Impedance spectra of the VRFC obtained for different levels of SOC; vanadium concentration of 0.125 M and stagnant electrolyte.

Fittings were performed for all the spectra measured, to validate the equivalent circuit model. Figure 5.15

shows the example of one of the fittings for a SOC of 16% with electrolyte circulation. A small tail at the low frequency end of the spectrum is observed in the experimental data, but was disregarded because of the low number of points and poor definition. The spectrum was fitted using two R-CPE networks, in which the one at high frequencies has poor definition (revealed by fitting errors well above 10%). The low frequency loop is well defined and the alpha-exponent (CPE-P) is above 0.9, thus a capacitance nature, assigned to the double layer capacitance at the electrode/electrolyte interface.

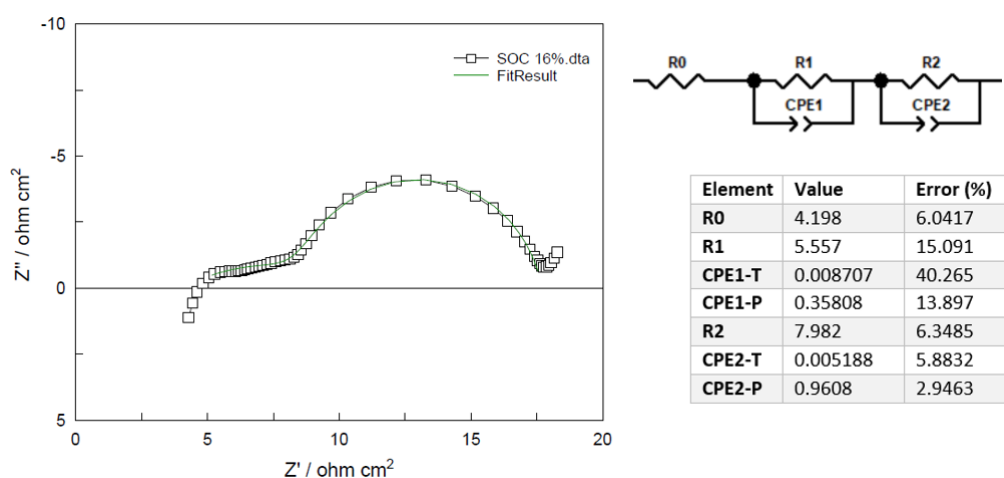


Figure 5.15: Fitting directly taken from ZView Software for the experimental results at 16% SOC for a vanadium concentration of 0.125 M (flow rate of 20.4 mL/min), where units for R are $\Omega \text{ cm}^2$, for CPE-T are $\text{F cm}^{-2}\text{s}^{\alpha-1}$, and CPE-P has no units.

The ohmic resistance, R0, seems practically independent from the state of charge, ranging from 4.2 and 4.8 $\Omega \text{ cm}^2$, which shows that the ohmic resistance is not significantly affected by the state of charge of the cell. The SOC affects essentially the mass transfer and reaction rates. In fact, as seen in Figure 5.16, the low frequency loop, R2, finds its lower value around 50% SOC and becomes higher as SOC deviates from half-charged mode. This is a tendency that many other authors' observed as well [75, 76, 73], but few were able to understand. One of the reasons for this behavior could be the existence of a multivalent cation that reaches its peak concentration at 50% SOC and enhances the rate of electron transfer at the positive electrode [76]. On the other hand, EIS consists of applying a very small sinusoidal signal, which will oscillate between a positive and negative signal, and more charged/discharged solutions will create more resistance for such a small potential to polarize in a certain direction.

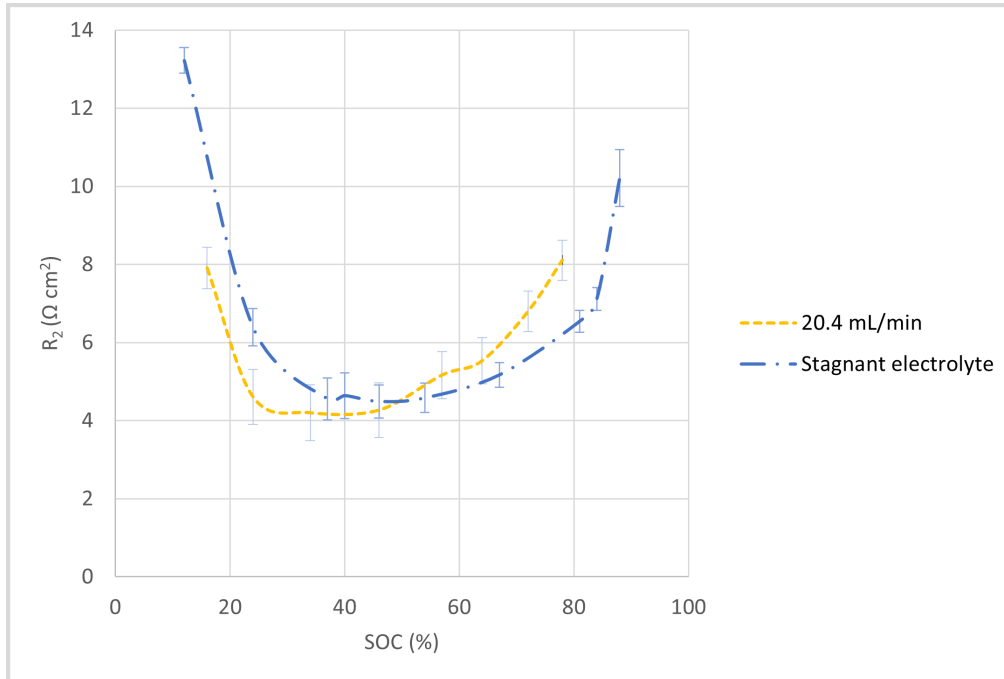


Figure 5.16: Evolution of R_2 with SOC with and without electrolyte circulation.

Considering both experiments, the tendency is the same and R_2 ranges from 3.8 to 13 $\Omega \text{ cm}^2$. The reaction rate will be maximum at SOC in a medium range, 30-70%, while the reaction seems to be slower at very high or very low SOC. For Li et al [49], these values ranged from 4.5 to 9.5 $\Omega \text{ cm}^2$, but for Becker et al [73] the values ranged from 0.45 to 0.7 $\Omega \text{ cm}^2$.

Number of felts

To study the effect of the active surface area on the charge-transfer resistance, impedance was measured when removing the carbon felts of both electrodes for a vanadium concentration of 1.21 M. The impedance should be inversely proportional to the active area of the electrode, as seen in Equation (3.2.2).

EIS data can be seen in Figure 5.17. Fittings were performed for both plots, using different circuit models, as it can be seen in Figure 5.18 and Figure 5.19. When no felts are present, the mass transport effects are represented in the EIS pattern as a straight line instead of a semi-circle, which corresponds to a transport across a semi-infinite diffusion layer. In this case, the spectra is best fitted to an open Warburg element.

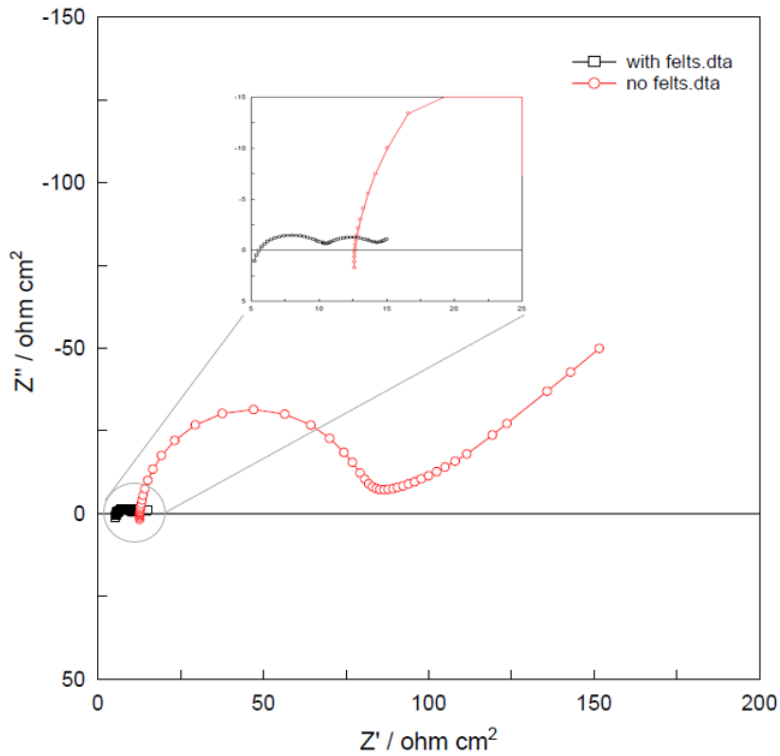


Figure 5.17: Impedance spectra of the VRFC with and without carbon felts; vanadium concentration of 1.21 M and flow rate of 20.4 mL/min.

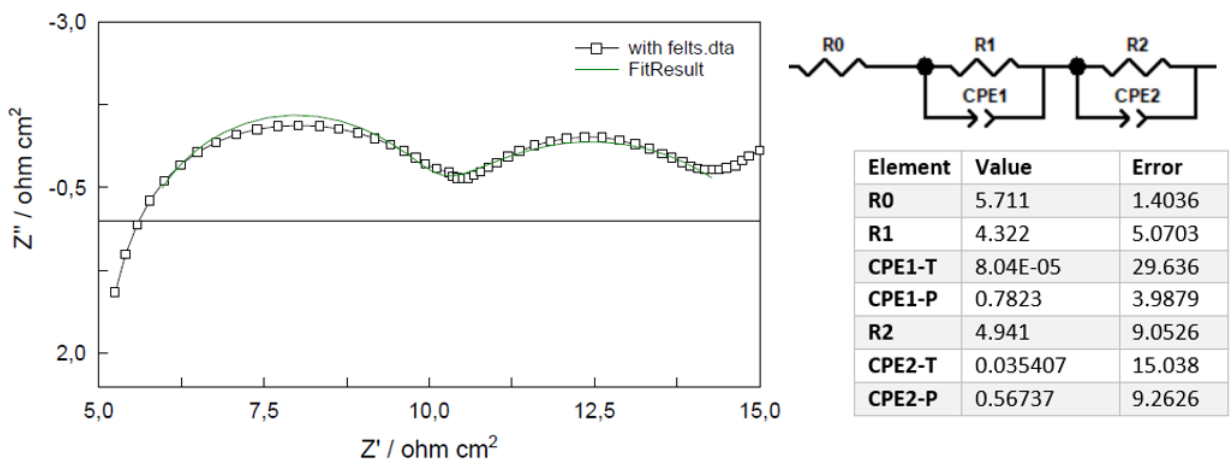


Figure 5.18: Fitting results directly taken from ZView Software for a cell with carbon felts (concentration of vanadium 1.21 M, flow-rate 20.4 mL/min), where units for R are $\Omega \text{ cm}^2$, for CPE-T are $\text{F cm}^{-2} \text{ s}^{\alpha-1}$, CPE-P has no units.

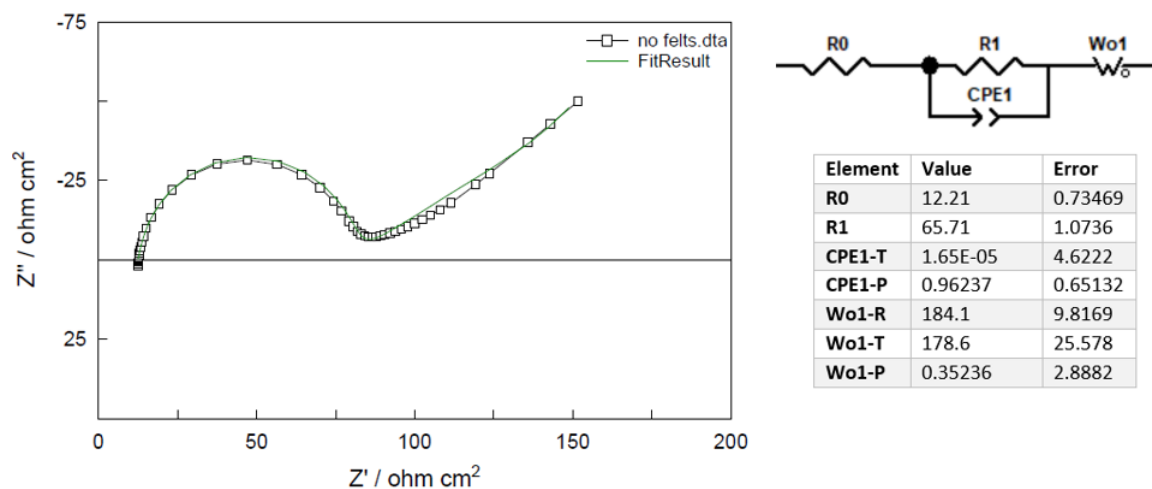


Figure 5.19: Fitting results directly taken from ZView Software for a cell without carbon felts (concentration of vanadium 1.21 M, flow-rate 20.4 mL/min), where units for R are $\Omega \text{ cm}^2$, for CPE-T are $\text{F cm}^{-2} \text{ s}^{\alpha-1}$, CPE-P has no units, Wo-R has units of $\Omega \text{ cm}^2 \text{ s}^{-0.5}$, Wo-T has units of s and Wo-P has no units.

Considering an active area of 25 cm^2 , the charge-transfer resistance was $65.7 \Omega \text{ cm}^2$ with no felts and $4.3 \Omega \text{ cm}^2$ with felts (the first semicircle was considered). Because the ratio between R_1 from both experiments was 15.2, this multiplier was applied to the "with felts" impedance. A subtraction of a resistor with 74.6Ω (the difference between the ohmic resistances) was then performed to try to overlap the two graphs, resulting in Figure 5.20.

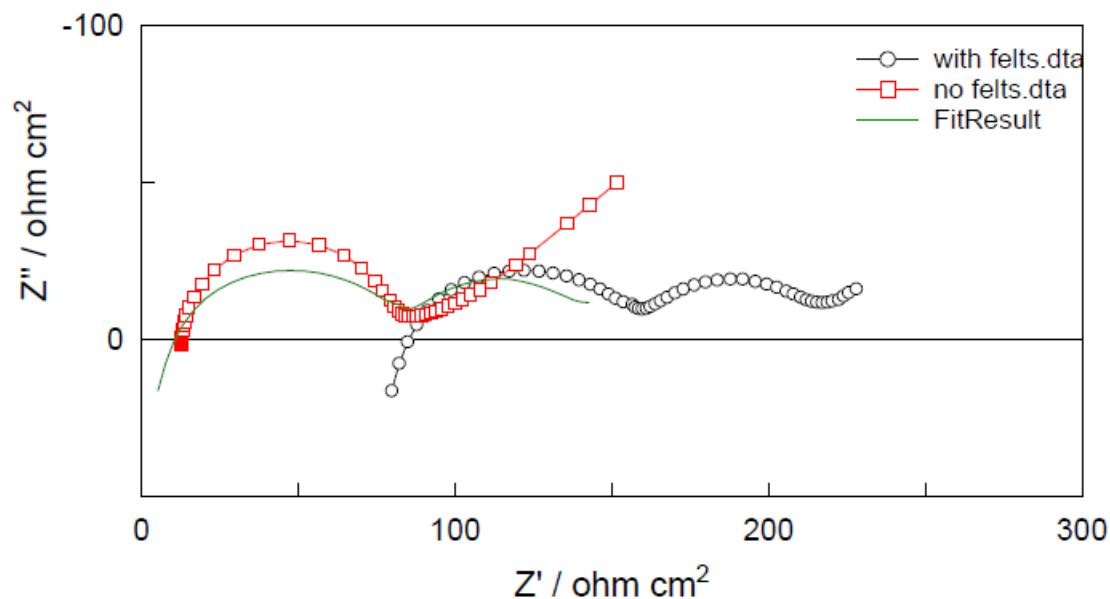


Figure 5.20: Impedance spectra of the VRFC with and without carbon felts, after applying a multiplier of 15.2 to "with felts" impedance and subtracting a 74.6Ω resistor; vanadium concentration of 1.21 M and flow rate of 20.4 mL/min.

The ratio between areas of both experiments was calculated to compare with the ratio of resistances. The supplier states that the felts' BET surface area, that is, the specific surface area, is of $0.8 \text{ m}^2/\text{g}$. For 3.5 felts of 25 cm^2 each, the mass is 7 g, which makes the real surface area of the electrodes around 5.6 m^2 . The ratio of areas with felts/no felts is then 225, which is higher than the ratio of resistances no felts/with felts, which is 15.2. Possibly the area is not the only factor affecting the charge-transfer resistance in this case. In a similar study using the same cell arrangement, with 3.5 vs 1 felts in each half-cell, the charge-transfer resistance was 3.5 times higher for the case in which only one felt was used. It means that when the area was changed but there were still carbon felts present in each experiment the inverse proportionality was verified, but when the area was changed and one of the experiments had no carbon felts and only the graphite plates, the proportionality was not verified. This suggests that the different materials, the graphite plate and the carbon felts, present different resistances on their own, independently from the area, the carbon felts presenting higher resistance.

Effect of concentration

The effect of the vanadium concentration in the cell's resistance was studied performing EIS measurements for the concentration of 1,21 M and 0.125 M, and the results can be seen in Figure 5.21. In Figure 5.22 the different resistances are presented, where R_0 is higher for the more concentrated elec-

trolyte, and R_1 and R_2 are lower.

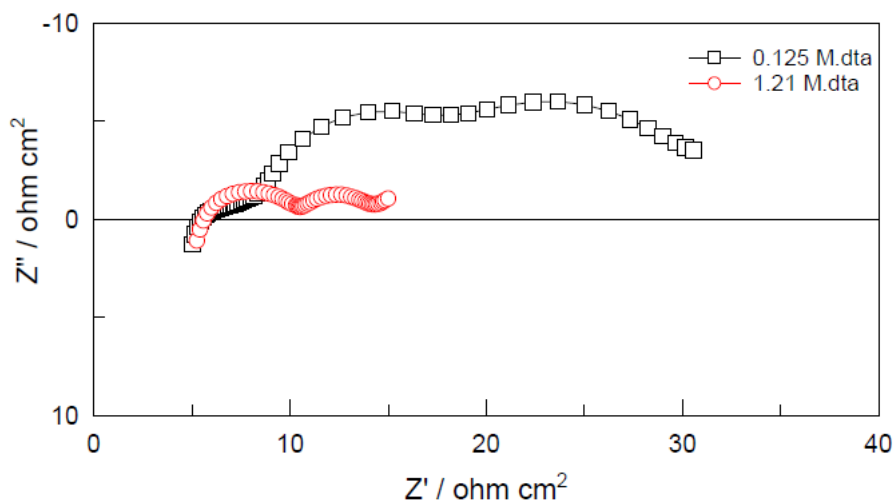


Figure 5.21: Impedance spectra of a VRFC for vanadium concentrations of 0.125 M and 1.21 M; flow rate of 20.4 mL/min.

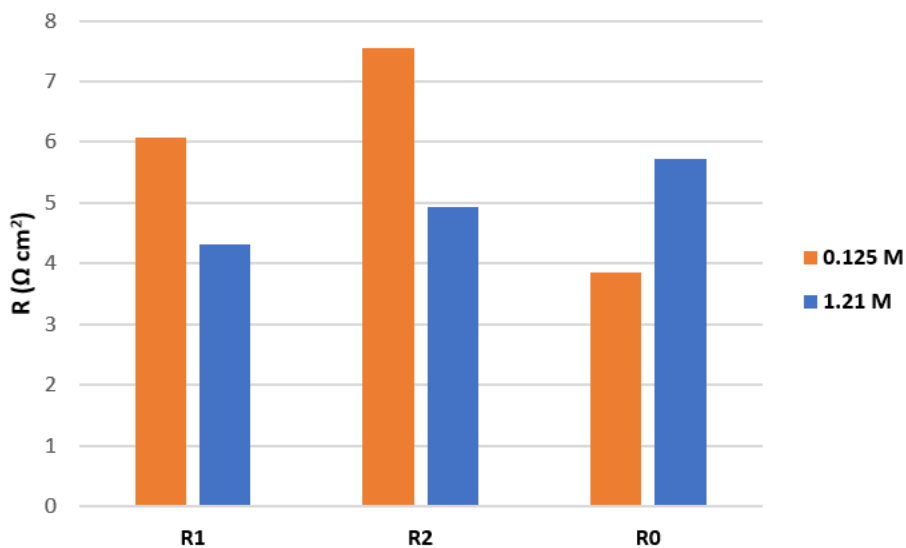


Figure 5.22: Values of R_0 , R_1 and R_2 for vanadium concentrations of 0.125 M and 1.21 M.

Overcharging

To be able to reach high values of SOC for previous experiments, the cell was overcharged at 2.2 V, which goes beyond the potential limit recommended, 1.8 V. After overcharging, corrosion of the positive electrode was observed. Sticking and removing tape on the corroded area showed that more particles

of carbon come off in comparison to a non-corroded electrode, as seen in Figure 5.23. The effect of corrosion on the cell's impedance was studied and EIS results for a SOC of 45% after overcharge are shown in Figure 5.24, where a semi-infinite linear transport appears at low frequencies.

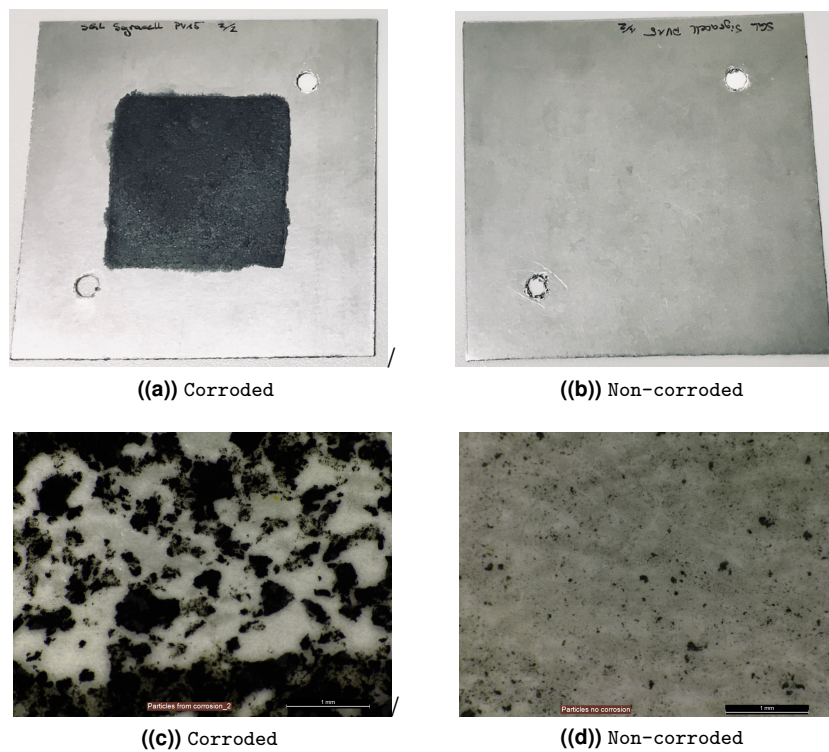


Figure 5.23: Graphite plates with (a) and without (b) corrosion and particles removed by the tape from the corroded electrode (c) and the non-corroded electrode (d).

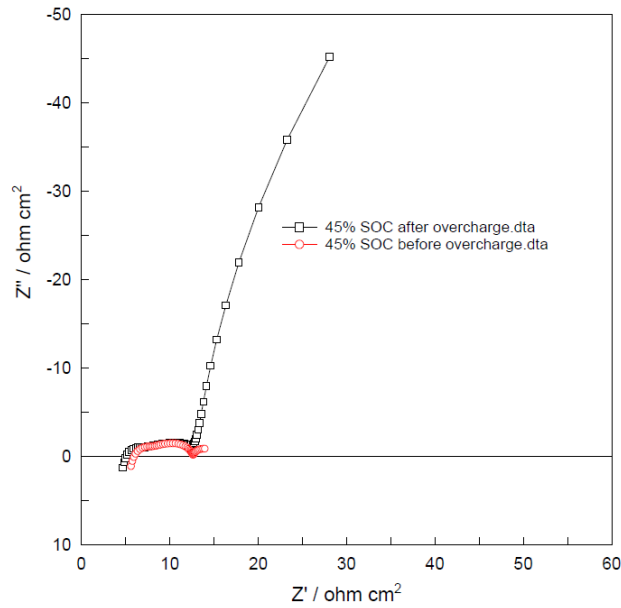


Figure 5.24: Impedance spectra obtained before and after overcharging the cell; 45% SOC and flow rate of 20.4 mL/min.

This spectrum was best fitted using a CPE element instead of a Warburg at low frequencies, as seen in Figure 5.25. A Warburg element and a CPE at 45° ($\alpha = 0.5$) are mathematically the same, which is why a CPE is often used to describe diffusion behavior as well. In this case, the value of CPE3-P greatly deviates from 0.5, which is probably due to the curvature reflected in the plot.

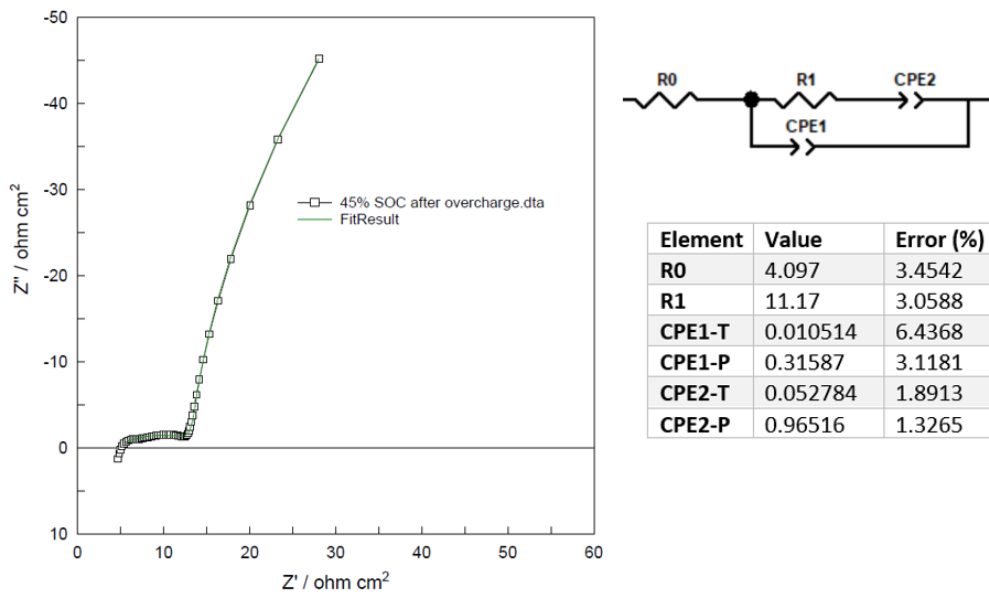


Figure 5.25: Fitting results directly taken from ZView Software for a 45% SOC after overcharging the cell at 2.2 V, where units for R are $\Omega \text{ cm}^2$, for CPE-T are $\text{F cm}^{-2} \text{ s}^{\alpha-1}$, and CPE-P has no units.

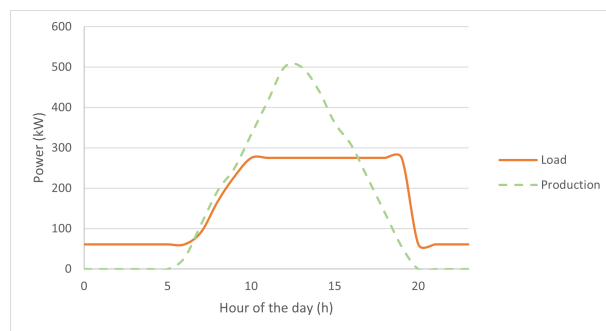
6

Economic Evaluation

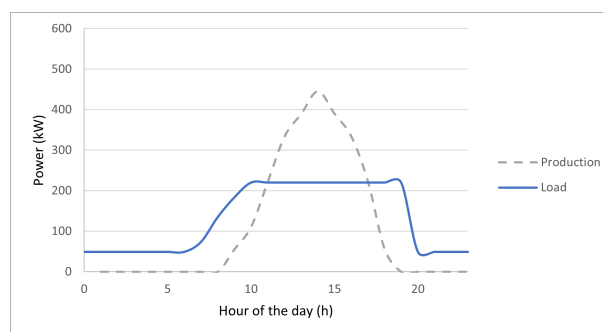
As useful as VRFB can be to reduce the use of fossil fuels at the utility-scale, they will only become appealing for the commercial/industrial sector if they are economically attractive. To assess the economic feasibility of installing a VRFB system in a commercial facility, a simulation was performed considering the big "Recheio" Supermarket from the company "Jerónimo Martins", in Tavira, Portugal. This unit was chosen because it already has a PV system installed in 2018, from which a good amount of data was gathered or based upon, and because in this location the solar radiation conditions are favourable all year round. Besides VRFB, other technologies such as Li-ion and lead-acid batteries were studied as well so to compare which battery is the best fit.

Residential, commercial and industrial consumers can take advantage of BESS for behind-the-meter purposes, which means, to be as independent from the grid as possible and reduce the electricity bill at the end of the month. This type of customer usually owns a set of PV panels for self-consumption,

or other source of energy, and the ESS serves to avoid resorting to the grid when the demand exceeds the self-production, specially during peak hours when the electricity price is higher. The daily load curve for the Recheio facility in both winter and summer, as well as the daily PV production, is presented in Figure 6.1. The load curves were created considering the typical shape for a commercial facility [28] and a total charge demand of 306 kW (max power consumption of the day). This was the power demand assumed because in 2018 Jerónimo Martins completed two PV system installation projects, one at the distribution center in Algoz [77] including 3876 panels and a peak power of 741 kWp, and 1600 PV panels in the unit of consideration, which correspond to a peak power of 306 kWp. For simplicity this was assumed to be the daily power demand for the facility. The PV production curves consider the natural evolution of solar radiation throughout the day and a peak power of 556 kWp. Extra 250 kWp were added to the existing 306 kWp for simulation purposes, because a commercial facility operates mostly during the day, when the sun radiation is at its peak, therefore extra PV panels are needed to capture extra energy and charge the batteries.



((a)) Summer



((b)) Winter

Figure 6.1: Typical load curve and solar production curve for summer and winter months. Power demand during the winter was considered to be 20% lower in comparison with summer.

In order to store the excess energy produced in summer, a 1 MWh with 250 kW nominal power battery was considered. The battery's round-trip efficiency, that is, the charge-discharge efficiency, affects the energy output so it should be taken into account when estimating the energy savings each month.

Another property that must be considered is the depth of discharge (DoD), because not all batteries can fully discharge without compromising the cell's performance, which reduces the energy output [30]. The initial investment required by each technology is also important. The capital expenditure (CAPEX), which is the capital needed to acquire the equipment [78] can sometimes be split into two: CAPEX_{BS} for the core battery, and CAPEX_{BoP} to account for the rest of the equipment, such as battery management system, cables and inverters. The total investment, INV, made during the installation of the battery system is then:

$$INV = CAPEX_{BS} * CAP + CAPEX_{BoP} * P_N \quad (6.0.1)$$

where CAP is the battery's total capacity in kWh and P_N stands for its nominal power in kW. Another parameter that will vary from battery to battery is its operation and maintenance costs (OM), which will dictate the amount of money spent on the battery each year. The parameters for the different types of batteries studied can be seen in Table 6.1.

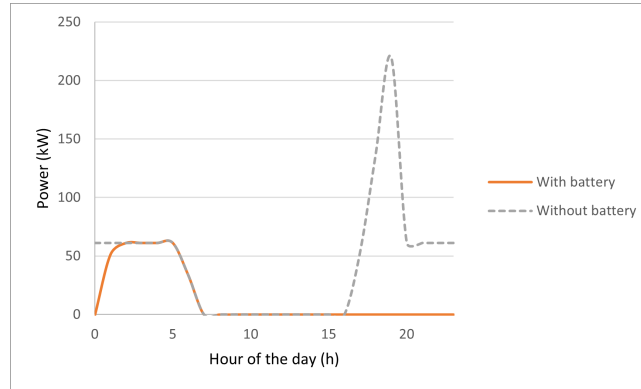
Table 6.1: Properties for each type of battery.

	VRFB	Ref.	Li-ion	Ref.	Lead-acid	Ref.
Efficiency (round-trip) (%)	72	[28]	91	[28]	86	[28]
DoD (%)	100	[30]	90	[30]	80	[28]
Life time (years)	20	[14]	10-20 ¹	[14]	10-20 ¹	[14]
CAPEX_{BS} (€/kWh)	124	[79]	288	[13]	206	[13]
CAPEX_{BoP} (€/kW)	1062 ²	[79]	495	[13]	485	[13]
O&M (% of Inv.)	7	[30]	5.6	[13]	7	[13]

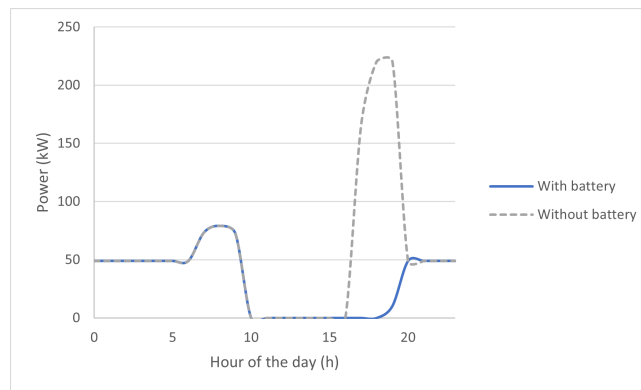
The power required from the grid throughout the day with and without the installation of VRFB batteries, for both winter and summer, is shown in Figure 6.2. In winter, batteries help reduce the power demanded from the grid between 4 and 8 p.m., while in summer this period is extended until 2 a.m. The total energy saved was computed to be 20 MWh/year in the winter and 25.4 MWh/year in the summer, giving a total annual energy savings of 45.4 MWh/year. Furthermore, the maximum power demanded from the grid decreases from 220 to 62 kW in winter and from 220 kW to 80 kW in summer.

¹10 years of life-time will be considered for calculations for the li-ion and lead-acid batteries.

²Here, 1000 €/kW are related to the stack costs, which are actually storage costs, but because they are specific to the power of the battery, it was decided to couple with the additional equipment parcel.



((a)) Summer



((b)) Winter

Figure 6.2: Power demanded to the grid during a) summer and b) winter when a VRFB is and is not installed.

The monthly electricity bill C_M depends on the total amount of energy requested to the grid E_M in kWh, the electricity cost c_{kWh} in €/kWh, the demand charge c_{kW} in €/kW-month and the peak power demand of the month in kW-month as follows:

$$C_M = c_{kWh} E_M + c_{kW} P_M \quad (6.0.2)$$

It was assumed that the company is billed through a two-hourly electricity tariff structured as follows [80]:

- On-peak hours (7 a.m. to 12 a.m.): $c_{kWh} = 0.25$ €/kWh;
- Off-peak hours (12 a.m to 7 a.m): $c_{kWh} = 0.1$ €/kWh;
- Demand-charge $c_{kW} = 2$ €/kW-month.

Annual savings will be the difference between the total cost of energy without the batteries and the total

cost with them. The annual savings only for the electricity bill, considering no capacity loss throughout the battery's life-time, is of 56 352 €/year. When considering the extra expenses related to the maintenance of the battery, the annual profit of this project becomes 29 089 €/year. To assess the economical feasibility of the installment project, the following parameters were calculated:

- **Net Present Value (NPV):** it is an estimate of the value for the investment project considering the effect of time over the value of money. If the NPV is positive at the end of the period of the project, the investment project is profitable [78];
- **Return on Investment (ROI):** this metric can have different interpretations. Here, the same interpretation made by Lorenzi et al [30] was made and it is the percentage of the initial investment that is recuperated each year, on average, during the duration of the project;
- **Internal Rate of Return (IRR):** Discount rate at which the NPV is zero. It is the annual rate of growth an investment is expected to generate [78]. It differs from the ROI because it takes into consideration the effect of time;
- **Payback Period:** the amount of time it takes to recover the cost of an investment [78].

Each year, the profit from this project will be the annual savings, that is, the difference between the electricity bill without, C_M , and with, C_{Mb} the batteries, minus the costs in operation and maintenance, O&M. The NPV is then calculated using the following expression, where r stands for the discount rate:

$$NPV = -INV + \sum_{n=1}^{12} \frac{C_M - C_{Mb} - O\&M}{(1+r)^n} \quad (6.0.3)$$

The discount rate is often the company's weighted average cost of capital (WACC), which strongly depends on the firm's capital debt and equity. For this study a discount rate of 3% was considered, which was used by other authors [28].

The results are shown in the Table 6.2. Only VRFB were able to reach a positive NPV over the time-span of the project, 20 years. The value of the project will be 11% of the initial investment, and after 20 years the equipment has to be replaced. Negative values of discount rate are needed for the NPV to be zero in the case of lead-acid and li-ion batteries, even though li-ion present the highest electricity bill savings per year.

Table 6.2: Economic parameters calculated for each BESS technology.

	VRFB	Li-ion	Lead-acid
NPV (€)	43 247	-206 258	-95 645
Bill savings (€/year)	56 352	57 499	55 321
ROI (%)	7.5	8.4	9.8
IRR (%)	4.2	-3.5	-0.45
Payback Period (years)	17	–	–

The highest ROI is found for the lead-acid batteries, which shows that if it weren't for the short life-time, these batteries would result in a positive NPV. As for the li-ion batteries, besides the short life-time, there are also high investment costs preventing the technology to break-even, even though its high round-trip efficiency.

When comparing results obtained by different authors, differences in the assumptions made for various parameters become apparent. Large differences in the initial investment for each technology are the most noticeable. In 2016, Graditi et al [28] studied the economic feasibility of different technologies in a large supermarket facility in Italy, for a project life of only 10 years with no battery replacement. They found that, at the current BESS prices, most technologies are not very cost effective and li-ion and flow batteries showed the better results, with lead-acid never breaking-even, probably due to the high costs assumed, higher than those for VRFB and LIB, which is not in agreement with other sources [13, 12]. In 2019, Lorenzi et al [30] studied different technologies for utility-scale application and concluded that the higher round-trip efficiency and lower maintenance costs presented by li-ion batteries is not sufficient to counterbalance the higher costs of investment. This study was performed considering a round-trip efficiency of 85% for VRFB, which is rather optimistic and deviates from most sources that state it to be around 75% [12, 14, 28]. On the other hand, Fisher et al [14] completely disagree with the economic competitiveness of VRFB. In their study, VRFB would have to significantly reduce its costs in order to break-even in comparison with lead-acid and li-ion batteries. Regardless of the different conclusions reached by different authors, the longevity of the VRFB is undeniably an important feature that sets its competitiveness in comparison with other technologies.

7

Discussion

The main objective of this work was to make an electrochemical characterization of the vanadium redox flow cell, based upon the EIS technique. Assembling of the cell proved to be a sensitive factor, as leaking of highly acidic electrolyte needs to be avoided. In order to prevent leaking, tightening of the screws should be done meticulously and gradually, following an order that means going in nearly diametrically opposed positions and preferably using an adjustable torque wrench. Because that was not available, screws were manually tightened and the process was not always successful, especially in the beginning of the experimental work. An initial set-up with two cells in series was attempted, with the goal of tracking the system's OCP throughout the measurements at the cell upstream. The two cells, however, had different geometry and material composition, which caused the two cells to hardly ever present the same OCP, probably due to the different distribution of electrolyte inside the cell, and the set-up was unfruitful. Nevertheless, had the two cells been similar, this would be a good way to have control over the OCP at which the EIS measurements were taken, and has already been successfully implemented

by other authors [49, 48].

One important point for the characterization of the cell was the determination of the formal potential, which indirectly depends on the composition of the solution. The method used in this work to compute the formal potential was similar to [48]. The computed value of 1.43 V is slightly higher than in the one determined by Haisch et al, 1.35 V [48], and Tang et al, 1.4 V [53]. These authors use different concentrations of vanadium and sulfuric acid, which can be the cause for deviations. On the other hand, it was assumed in this method that for the same current density the overpotential of charge and discharge curves is the same for a given SOC, only symmetrical, which in reality may not be true. The kinetics of the different reactions in both directions are certainly different, although several authors reach different conclusions as to which reaction in each half-cell is the slowest. On the other hand, it is also assumed that each charge/discharge curve itself is symmetrical and the middle point will be at 50% SOC, which can also deviate from the truth since the viscosity of the solution changes with its composition in vanadium ions: a solution of VO^{2+} is more viscous, followed by a VO_2^+ solution, then a V^{3+} solution and, finally, V^{2+} solution as seen by Blanc [9]. A more rigorous method for the determination of the formal potential would be to verify the concentration of ions by titration and measure the potential when all vanadium species are present in the same proportion.

Good coulombic efficiency above 96% was achieved during charge/discharge processes in the cell, in agreement with results obtained by Wang et al [69]. However, charge/discharge curves while circulating the electrolyte were inconclusive: a cut-off voltage of 1.8 V was imposed, in order to prevent overcharging, but was achieved inside the cell before the electrolyte in the tanks was fully charged, specially for currents above 4 mA/cm^2 , possibly due to mass transport issues in the felts. For higher currents, charging in steps was an option, and current densities were frequently below the current values claimed in the literature, of 25 to 100 mA/cm^2 [48, 81]. Besides, both polarization curves and EIS measurements showed that the ohmic resistance of the cell studied in this work is higher than the one seen by other authors [3], which will also contribute for lower currents.

Polarization curves showed a 17% increase of current limit for a flow rate variation of 9.4 to 20.4 mL/min, in agreement with the results obtained by Aaron et al [3]. For a higher flow rate, the vanadium active species do not get depleted as fast at the electrode surface, which makes mass transfer limitations occur only at a much greater current. For higher concentrations of electrolyte the high amount of vanadium species seems to avoid mass transport issues altogether. When designing a VRFB, it is important to consider both the advantages of improving the cell's performance by working at high flow rate and the losses coming from worse electrolyte utilization and more energy required by the pump.

Despite the ease of operation in what concerns the EIS technique, there were also a few difficulties. Although in subsequent measurements the spectra usually revealed trends, reproducibility was far from perfect. There are several possible explanations for that, including different properties at the surface of the electrodes due to corrosion, different contact resistance at the current collectors due to oxidation, and different distribution of the electrolyte inside the cell. Nevertheless, valid conclusions were taken from EIS results and this technique allowed to better understand the behaviour of the cell under different experimental conditions.

Nyquist plots for a vanadium concentration of 0.125 M including carbon felts in the cell's assembly presented an odd shape at high frequencies. Except for the removal of carbon felts and utilization of a different electrolyte, no other experimental conditions seemed to affect the irregular shape observed, which was therefore considered irrelevant for the interpretation of the rest of the spectrum. Although no exact explanation for the weird shape at high frequencies was found, it is suspected to be related to the contact between the carbon felts and the solution, specifically when this solution has low concentration.

The ohmic resistance, reflected at the plot's intersection with the horizontal axis at high frequencies, is directly proportional to the number of membranes included in the cell's assembly. These results confirm that the main process contributing to the cell's ohmic resistance is the H⁺ transfer through the membrane, a process that will show higher resistance if more membranes are added. Deviations from a perfect linear relationship can be explained by the fact that increasing the number of membranes forces the protons to go through a small distance of solution in between them, which is not the same as simply increasing the membrane thickness. The fact that lower values of ohmic resistance were achieved by other authors shows that the cell's set up can be optimized. The membrane being the main component contributing for this impedance, the key factor is possibly related to its activation process, which could be optimized, where essential sulfur channels for the proper transfer of protons are activated. Accumulation of oxides on the copper current collectors can influence the cell's ohmic resistance, which is why it was important to polish the copper at every assembly process of the cell. Other factors, such as solution resistance and ohmic resistance of wires and current collectors, appear to account for only 3% of the total ohmic resistance of the cell, which is 3.9 Ωcm^2 . The ohmic resistance of the cell did not vary with and without electrolyte circulation, which means that the proton exchange does not get affected by the circulation of electrolyte. EIS results show an increase in the ohmic resistance from 3.9 Ωcm^2 to 5.7 Ωcm^2 when the vanadium concentration of the electrolyte increases from 0.125 M to 1.21 M, which oddly enough goes against the results obtained from the polarization curves, in which a decrease in resistance was observed. However, EIS is believed to be a more exact technique. The viscosity of the solution increases with its concentration, which affects the mobility of the ions and increases the ohmic

resistance. The charge-transfer resistance, on the other hand, decreases with a more concentrated electrolyte, possibly due to the high amount of available species at the electrodes' surface.

Two capacitive loops are usually observed in Nyquist plots, the high frequency one being related to the cell's charge-transfer resistance and the low frequency one to mass-transport effects. When studying the effect of SOC in the cell's impedance, only one arc was observed instead of two. When only one arc is observed, mass transport effects may be only present at very low frequencies, or their contribution is reflected on the singular semi-circle which is accounting for both charge-transfer and mass transport, something that has been said to occur when the optimization of the vanadium ions concentration and the supporting electrolyte is not achieved [65].

Mass transport effects were reflected in the EIS patterns differently for different experimental conditions. They were mostly represented by a second capacitive loop at low frequencies, accounted for in the circuit model by a RC parallel network and showing that in those situations the transport of vanadium ions through the porous electrodes is more significant than diffusion from the bulk of the solution to the interface. In the experiment where no carbon felts were used at a vanadium concentration of 1.21 M, however, the spectra at low frequencies is best fitted to a Warburg element, which makes sense because without carbon felts there is no internal mass transport and the diffusion of vanadium ions from the bulk of the solution to the electrode is the significant mass transport effect. When studying the corrosion of the positive electrode, external mass transport effects were also observed in the spectra, but with some deviations from the regular Warburg-type straight line, probably because a mixture of the two processes is present. Enhanced diffusion effects after over-charging of the cell were also observed by Sun et al [74].

When assessing the economic feasibility of installing a VRFB system in a commercial facility in Tavira, a positive NPV of 43 247 € was reached, supporting the profitability of the project. The final value of the project is small, but environmental benefits considering more solar energy is being used stand as another attractive point supporting its realization. Other electrochemical batteries did not show positive NPV, and the great competitiveness show by VRFB is clearly attributed to the extended life-time, a key factor that is able to compensate for the low efficiency and relatively high costs of investment. This specific case study was carried considering a commercial facility aiming to decrease its electricity bill while making the best out of its PV panels. However, commercial facilities already take good advantage of their PV installations without BESS, as their periods of highest consumption overlap with the periods of peak radiation. Extra PV panels are needed in order to charge the batteries, which is a cost that was not considered in this work. Another way to reduce the electricity bill, uncoupled from the PV production,

would be to charge the batteries overnight when the electricity price is lower and discharge it during the day when the price is higher, also helping to reduce the power charge demand. When coupled with a PV installation, BESS are probably best suited for residential applications, where peak consumption occurs during the evening, and for utility-scale purposes, where the extra energy stored by BESS can be used to supply the grid during the evening as well without resorting to fossil fuels.

8

Conclusions

Electrochemical Impedance Spectroscopy proved to be a successful technique to study the electrochemical behaviour of the cell without disrupting the properties of the system in each measurement, and multiple valid conclusions were gathered. The ohmic resistance of the cell for the standard experimental set-up and a vanadium concentration of 0.125 M was $3.9 \Omega \text{ cm}^2$, with the resistance of the Dupont Nafion 117 membrane treated as such being $3.8 \Omega \text{ cm}^2$. The charge-transfer resistance ranged from 3.8 to $13 \Omega \text{ cm}^2$, and results showed that lower impedance will be found at a range of 30-70% SOC. Mass transport effects changed for different experimental conditions. With the removal of the carbon felts semi-infinite linear behaviour for mass transport is observed. At the presence of carbon felts, a finite transport behaviour is observed.

An economic evaluation was performed considering the installation of a VRFB system at the "Recheio" Supermarket in Tavira. The VRFB installation promises to be successful if a 20 year time-span is con-

sidered while li-ion and lead-acid batteries don't, mostly due to their need of replacement after 10 years. The extended life-time and depth of discharge represent a huge advantage for VRFB, but other properties such as their round-trip efficiency and investment costs are a lay-up. Future developments in this technology, alongside a reduction in costs, will solidify the role of VRFB as a good energy storage solution for stationary applications.

9

Perspectives for Future Work

As this project reaches the end, several remarks as to what future work can be performed around the topic can be made. The initial set up attempted, with two equal cells assembled in series to track the system's SOC and OCP in real-time, while testing one of the cells, would be very helpful. Further EIS analysis should be performed, as several hardships encountered during the experimental testing decreased the time available to perform other some more measurements. Testing each half-cell separately would be helpful to further how the internal losses of the cell are distributed, for example. Some improvements in assembly could be attempted, including a more efficient method for membrane activation, the utilization of high concentrated electrolyte and having the copper current collectors gold plated to avoid the accumulation of oxides that increases the cell's ohmic resistance. Different geometries for the cell should be studied and higher flow rates achieved, to attempt to increase the current density allowed during operation of the cell. Ultimately, the goal would be to perform tests on a successfully assembled battery stack with two cells.

References

- [1] A. Clemente, G. A. Ramos, and R. Costa-Castelló, "Voltage Control of a Vanadium Redox Flow Battery," *Electronics*, pp. 1–24, 2020. [Online]. Available: www.mdpi.com/journal/electronics
- [2] J. Fu, M. Zheng, X. Wang, J. Sun, and T. Wang, "Flow-Rate Optimization and Economic Analysis of Vanadium Redox Flow Batteries in a Load-Shifting Application," *Journal of Energy Engineering*, vol. 143, no. 6, pp. 1–13, 2017. [Online]. Available: <https://ascelibrary.org/doi/10.1061/%28ASCE%29EY.1943-7897.0000493>
- [3] D. Aaron, Z. Tang, A. B. Papandrew, and T. A. Zawodzinski, "Polarization curve analysis of all-vanadium redox flow batteries," *Journal of Applied Electrochemistry*, vol. 41, no. 10, pp. 1175–1182, 2011. [Online]. Available: <https://doi.org/10.1007/s10800-011-0335-7>
- [4] A. R. L. Middlemiss, "Characterisation of batteries by electrochemical impedance spectroscopy," *Energy Reports*, vol. 6, pp. 232–241, 2020. [Online]. Available: <https://doi.org/10.1016/j.egy.2020.03.029>
- [5] M. Uddin, M. F. Romlie, M. F. Abdullah, S. Abd Halim, A. H. Abu Bakar, and T. Chia Kwang, "A review on peak load shaving strategies," *Renewable and Sustainable Energy Reviews*, vol. 82, no. November 2017, pp. 3323–3332, 2018. [Online]. Available: <https://doi.org/10.1016/j.rser.2017.10.056>
- [6] J. P. Chamberlain, R. Hammerschlag, and C. P. Schaber, "Energy Storage Technologies," in *Energy Efficiency and Renewable Energy Handbook*, D. Y. Goswami, Ed. Boca Raton: CRC Press, 2016, pp. 939–966.
- [7] B. Zohuri, *Hybrid Energy Systems: Driving Reliable Renewable Sources of Energy Storage*. Albuquerque, NM, USA: Springer, 2017.

- [8] H. Zhang, "Large Scale Energy Storage: An Overview," in *Redox Flow Batteries: Fundamentals and Applications*, J. Z. Huamin Zang, Xianfeng Li, Ed. Boca Raton: CRC Press, 2018, ch. 1, pp. 2–39.
- [9] C. Blanc, "Modeling of a Vanadium Redox Flow Battery for Energy Storage," *École Polytechnique Fédérale de Lausanne*. [Online]. Available: <https://infoscience.epfl.ch/record/129758>
- [10] A. Immendoerfer, I. Tietze, H. Hottenroth, and T. Viere, "Life-cycle impacts of pumped hydropower storage and battery storage," *International Journal of Energy and Environmental Engineering*, vol. 8, no. 3, pp. 231–245, 2017. [Online]. Available: <https://doi.org/10.1007/s40095-017-0237-5>
- [11] Z. Ma, G. C. Glatzmaier, and C. F. Kutscher, "Thermal energy storage and its potential applications in solar thermal power plants and electricity storage," *ASME 2011 5th International Conference on Energy Sustainability, ES 2011*, no. PARTS A, B, AND C, pp. 447–456, 2011. [Online]. Available: <https://doi.org/10.1115/ES2011-54077>
- [12] G. J. May, A. Davidson, and B. Monahov, "Lead batteries for utility energy storage: A review," *Journal of Energy Storage*, vol. 15, pp. 145–157, 2018. [Online]. Available: <http://dx.doi.org/10.1016/j.est.2017.11.008>
- [13] E. Lockhart, X. Li, S. Booth, J. Salasovich, D. Olis, J. Elsworth, and L. Lisell, "Comparative Study of Techno-economics of Lithium-ion and Lead-acid Batteries in Micro-grids in Sub-Saharan Africa," National Renewable Energy Laboratory, Tech. Rep., 2019. [Online]. Available: <https://www.nrel.gov/docs/fy19osti/73238.pdf>
- [14] M. Fisher, J. Apt, and J. F. Whitacre, "Can flow batteries scale in the behind-the-meter commercial and industrial market? A techno-economic comparison of storage technologies in California," *Journal of Power Sources*, vol. 420, no. March, pp. 1–8, 2019. [Online]. Available: <https://doi.org/10.1016/j.jpowsour.2019.02.051>
- [15] A. R. Dehghani-Sani, E. Tharumalingam, M. B. Dusseault, and R. Fraser, "Study of energy storage systems and environmental challenges of batteries," *Renewable and Sustainable Energy Reviews*, vol. 104, no. November 2018, pp. 192–208, 2019. [Online]. Available: <https://doi.org/10.1016/j.rser.2019.01.023>
- [16] D. Deng, "Li-ion batteries: basics, progress, and challenges," *Energy Science & Engineering*, vol. 3, no. 5, pp. 385–418, 2015. [Online]. Available: <https://onlinelibrary.wiley.com/doi/abs/10.1002/ese3.95>

- [17] T. Chen, Y. Jin, H. Lv, A. Yang, M. Liu, B. Chen, Y. Xie, and Q. Chen, "Applications of Lithium-Ion Batteries in Grid-Scale Energy Storage Systems," *Transactions of Tianjin University*, vol. 26, no. 3, pp. 208–217, 2020. [Online]. Available: <https://doi.org/10.1007/s12209-020-00236-w>
- [18] W. Li, S. Lee, and A. Manthiram, "High-Nickel NMA: A Cobalt-Free Alternative to NMC and NCA Cathodes for Lithium-Ion Batteries," *Advanced Materials*, vol. 32, no. 33, 2020. [Online]. Available: <https://onlinelibrary.wiley.com/doi/abs/10.1002/adma.202002718>
- [19] Y. Chen, Y. Kang, Y. Zhao, L. Wang, J. Liu, Y. Li, Z. Liang, X. He, X. Li, N. Tavajohi, and B. Li, "A review of lithium-ion battery safety concerns: the issues, strategies, and testing standards," *Journal of Energy Chemistry*, 2020. [Online]. Available: <http://www.sciencedirect.com/science/article/pii/S2095495620307075>
- [20] L. V. Thomas, O. Schmidt, A. Gambhir, S. Few, and I. Staffell, "Comparative life cycle assessment of lithium-ion battery chemistries for residential storage," *Journal of Energy Storage*, vol. 28, no. September 2019, p. 101230, 2020. [Online]. Available: <https://doi.org/10.1016/j.est.2020.101230>
- [21] C. Ponce de León, A. Frías-Ferrer, J. González-García, D. A. Szánto, and F. C. Walsh, "Redox flow cells for energy conversion," *Journal of Power Sources*, vol. 160, no. 1, pp. 716–732, 2006. [Online]. Available: <https://doi.org/10.1016/j.jpowsour.2006.02.095>
- [22] Y. A. Gandomi, D. S. Aaron, J. R. Houser, M. C. Daugherty, J. T. Clement, A. M. Pezeshki, T. Y. Ertugrul, D. P. Moseley, and M. M. Mench, "Critical Review—Experimental Diagnostics and Material Characterization Techniques Used on Redox Flow Batteries," *Journal of The Electrochemical Society*, vol. 165, no. 5, pp. A970–A1010, 2018. [Online]. Available: <https://doi.org/10.1149/2.0601805jes>
- [23] W. Wang, J. Kizewski, and W. Duan, "Introduction to Redox Flow Batteries," in *Redox Flow Batteries: Fundamentals and Applications*, J. Z. Huamin Zang, Xianfeng Li, Ed. Boca Raton: CRC Press, 2018, ch. 2, pp. 43–76.
- [24] A. Z. Weber, M. M. Mench, J. P. Meyers, P. N. Ross, J. T. Gostick, and Q. Liu, "Redox flow batteries: A review," *Journal of Applied Electrochemistry*, vol. 41, no. 10, pp. 1137–1164, 2011. [Online]. Available: <https://doi.org/10.3390/molecules201119711>
- [25] W. Li, R. Zaffou, C. C. Sholvin, M. L. Perry, and Y. She, "Vanadium Redox-Flow-Battery Electrolyte Preparation with Reducing Agents," *ECS Transactions*, vol. 53, no. 7, pp. 93–99, 2013. [Online]. Available: <https://doi.org/10.1149/05307.0093ecst>

- [26] J. Martin, K. Schafner, and T. Turek, "Preparation of Electrolyte for Vanadium Redox-Flow Batteries Based on Vanadium Pentoxide," *Energy Technology*, vol. 8, no. 9, 2020. [Online]. Available: <https://doi.org/10.1002/ente.202000522>
- [27] A. Colthorpe, "51MWh vanadium flow battery system ordered for wind farm in northern Japan," <https://www.energy-storage.news/news/51mwh-vanadium-flow-battery-system-ordered-for-wind-farm-in-northern-japan>.
- [28] E. Telaretti, G. Graditi, M. G. Ippolito, and G. Zizzo, "Economic feasibility of stationary electrochemical storages for electric bill management applications: The Italian scenario," *Energy Policy*, vol. 94, pp. 126–137, 2016. [Online]. Available: <http://dx.doi.org/10.1016/j.enpol.2016.04.002>
- [29] G. Caralis, K. Rados, and A. Zervos, "On the market of wind with hydro-pumped storage systems in autonomous Greek islands," *Renewable and Sustainable Energy Reviews*, vol. 14, no. 8, pp. 2221–2226, 2010. [Online]. Available: <http://www.sciencedirect.com/science/article/pii/S136403211000047X>
- [30] G. Lorenzi, R. da Silva Vieira, C. A. Santos Silva, and A. Martin, "Techno-economic analysis of utility-scale energy storage in island settings," *Journal of Energy Storage*, vol. 21, no. January 2019, pp. 691–705, 2019. [Online]. Available: <https://doi.org/10.1016/j.est.2018.12.026>
- [31] G. Notton, D. Mistrushi, L. Stoyanov, and P. Berberri, "Operation of a photovoltaic-wind plant with a hydro pumping-storage for electricity peak-shaving in an island context," *Solar Energy*, vol. 157, pp. 20–34, 2017. [Online]. Available: <http://www.sciencedirect.com/science/article/pii/S0038092X17306850>
- [32] "Tasmanian Island to be King of Renewable Energy," 2012, <https://www.ecoult.com/images/press-releases/Read-more5.pdf>, last accessed on 17/11/2020.
- [33] R. Rapier, "Why Vanadium Flow Batteries May Be The Future Of Utility-Scale Energy Storage," 2020, <https://www.forbes.com/sites/rrapier/2020/10/24/why-vanadium-flow-batteries-may-be-the-future-of-utility-scale-energy-storage/?sh=7dedeaa62305>, last accessed on 17/11/2020.
- [34] M. A. Pellow, H. Ambrose, D. Mulvaney, R. Betita, and S. Shaw, "Research gaps in environmental life cycle assessments of lithium ion batteries for grid-scale stationary energy storage systems: End-of-life options and other issues," *Sustainable Materials and Technologies*, vol. 23, 2020. [Online]. Available: <http://www.sciencedirect.com/science/article/pii/S2214993718302318>

- [35] "The future of energy independence." 2020, <https://vrbenenergy.com/global-customers/#c>, last accessed on 17/11/2020.
- [36] M. Skyllas-Kazacos, M. Rychcik, R. G. Robins, and A. G. Fane, "New All-Vanadium Redox Flow Cell," *Journal of The Electrochemical Society*, no. May, pp. 1057–1064, 1986.
- [37] "Storage system tested at Sorne Hill wind farm in Donegal, Ireland," 2006, <https://www.windpowermonthly.com/article/961816/storage-system-tested-sorne-hill-wind-farm-donegal-ireland>, last accessed on 17/11/2020.
- [38] "VRB Energy Wins Contract for the Largest Vanadium Flow Battery in China for Energy Storage," 2020, <https://vrbenenergy.com/vrb-energy-wins-contract-for-the-largest-vanadium-flow-battery-in-china-for-energy-storage/>, last accessed on 17/11/2020.
- [39] "California Energy Commission picks vanadium instead of lithium batteries for major storage project," 2020, <https://www.power-technology.com/news/california-energy-commission-picks-vanadium-instead-of-lithium-batteries-for-major-storage-project/>, last accessed on 17/11/2020.
- [40] "COMMERCIAL INDUSTRIAL (CI)," 2020, <https://redflow.com/applications/commercial-industrial/>, last accessed on 06/12/2020.
- [41] Deloitte, "Energy storage: tracking the technologies that will transform the power sector," 2016, <https://www2.deloitte.com/content/dam/Deloitte/no/Documents/energy-resources/energy-storage-tracking-technologies-transform-power-sector.pdf>, last accessed on 28/10/2020.
- [42] F. Nadeem, S. M. Hussain, P. K. Tiwari, A. K. Goswami, and T. S. Ustun, "Comparative review of energy storage systems, their roles, and impacts on future power systems," *IEEE Access*, vol. 7, no. December 2018, pp. 4555–4585, 2019. [Online]. Available: <https://doi.org/10.1109/ACCESS.2018.2888497>
- [43] A. Crawford, V. Viswanathan, D. Stephenson, W. Wang, E. Thomsen, D. Reed, B. Li, P. Balducci, M. Kintner-Meyer, and V. Sprenkle, "Comparative analysis for various redox flow batteries chemistries using a cost performance model," *Journal of Power Sources*, vol. 293, pp. 388–399, 2015. [Online]. Available: <http://dx.doi.org/10.1016/j.jpowsour.2015.05.066>
- [44] M. Moore, M. Zhang, J. S. Watson, T. A. Zawodzinski, and R. M. Counce, "Capital Cost Sensitivity Analysis of an All-Vanadium Redox-Flow Battery," *Journal of The Electrochemical Society*, vol. 159, no. 8, pp. A1183–A1188, 2012. [Online]. Available: <http://dx.doi.org/10.1149/2.041208jes>

- [45] G. Ghirlanda, "Development of a Vanadium Redox Flow Battery for Energy Storage," *Instituto Superior Técnico, Universidade de Lisboa, Lisboa, Portugal*. [Online]. Available: https://www.researchgate.net/publication/334654277_Development_of_a_Vanadium_Redox_Flow_Battery_for_Energy_Storage
- [46] B. Arribas, R. Melicio, J. Ginja Teixeira, and V. Mendes, "Vanadium redox flow battery storage system linked to the electric grid," *Renewable Energy and Power Quality Journal*, 05 2016. [Online]. Available: <http://dx.doi.org/10.24084/repqj14.561>
- [47] C. A. Vincent and B. Scrosati, *Modern Batteries*, 2nd ed. Linacre House, Jordan Hill, Oxford OX2 8DP: Butterworth-Heinemann, 1997.
- [48] T. Haisch, H. Ji, and C. Weidlich, "Monitoring the state of charge of all-vanadium redox flow batteries to identify crossover of electrolyte," *Electrochimica Acta*, vol. 336, 2020. [Online]. Available: <https://doi.org/10.1016/j.electacta.2019.135573>
- [49] Y. Li, J. Bao, M. Skyllas-Kazacos, M. P. Akter, X. Zhang, and J. Fletcher, "Studies on dynamic responses and impedance of the vanadium redox flow battery," *Applied Energy*, vol. 237, no. June 2018, pp. 91–102, 2019. [Online]. Available: <https://doi.org/10.1016/j.apenergy.2019.01.015>
- [50] Z. Liu and Y. Zou, "Vanadium Flow Batteries: Principles, Characteristics, Structure, Evaluation," in *Redox Flow Batteries: Fundamentals and Applications*, J. Z. Huamin Zang, Xianfeng Li, Ed. Boca Raton: CRC Press, 2018, ch. 3, pp. 77–126.
- [51] T. Jirabovornwisut and A. Arpornwichanop, "A review on the electrolyte imbalance in vanadium redox flow batteries," *International Journal of Hydrogen Energy*, vol. 44, no. 45, pp. 24 485–24 509, 2019. [Online]. Available: <https://doi.org/10.1016/j.ijhydene.2019.07.106>
- [52] H. Liu, Q. Xu, C. Yan, and Y. Qiao, "Corrosion behavior of a positive graphite electrode in vanadium redox flow battery," *Electrochimica Acta*, vol. 56, no. 24, pp. 8783–8790, 2011. [Online]. Available: <http://www.sciencedirect.com/science/article/pii/S0013468611011297>
- [53] A. Tang, J. Bao, and M. Skyllas-Kazacos, "Dynamic modelling of the effects of ion diffusion and side reactions on the capacity loss for vanadium redox flow battery," *Journal of Power Sources*, vol. 196, no. 24, pp. 10 737–10 747, 2011. [Online]. Available: <http://www.sciencedirect.com/science/article/pii/S0378775311017095>
- [54] K. Ngamsai and A. Arpornwichanop, "Investigating the air oxidation of V(II) ions in a vanadium redox flow battery," *Journal of Power Sources*, vol. 295, pp. 292–298, 2015. [Online]. Available: <http://www.sciencedirect.com/science/article/pii/S0378775315300483>

- [55] T. Sukkar and M. Skyllas-Kazacos, "Water transfer behaviour across cation exchange membranes in the vanadium redox battery," *Journal of Membrane Science*, vol. 222, no. 1, pp. 235–247, 2003. [Online]. Available: <http://www.sciencedirect.com/science/article/pii/S0376738803003090>
- [56] S. Corcuera and M. Skyllas-Kazacos, "State-of-Charge Monitoring and Electrolyte Rebalancing Methods for the Vanadium Redox Flow Battery," *European Chemical Bulletin*, vol. 1, no. 12, pp. 511–519, 2012. [Online]. Available: <http://www.eurchembull.com/index.php/ECB/article/view/139/174>
- [57] N. Soohyun, L. Dongyoung, C. Ilbeom, and L. Dai Gil, "Smart cure cycle for reducing the thermal residual stress of a co-cured E-glass/carbon/epoxy composite structure for a vanadium redox flow battery," *Composite Structures*, vol. 120, pp. 107–116, 2015. [Online]. Available: <http://dx.doi.org/10.1016/j.compstruct.2014.09.037>
- [58] J. Xiong, M. Jing, A. Tang, X. Fan, J. Liu, and C. Yan, "Mechanical modelling and simulation analyses of stress distribution and material failure for vanadium redox flow battery," *Journal of Energy Storage*, vol. 15, pp. 133–144, 2018. [Online]. Available: <http://dx.doi.org/10.1016/j.est.2017.11.011>
- [59] N. Elgrishi, K. J. Rountree, B. D. McCarthy, E. S. Rountree, T. T. Eisenhart, and J. L. Dempsey, "A Practical Beginner's Guide to Cyclic Voltammetry," *Journal of Chemical Education*, vol. 95, no. 2, pp. 197–206, 2018. [Online]. Available: <https://pubs.acs.org/doi/10.1021/acs.jchemed.7b00361>
- [60] "Polarization Curves: setup, recording, processing and features," 2020, <https://www.palmsenscorrosion.com/knowledgebase/polarization-curves/>, last accessed on 04/12/2020.
- [61] D. V. Ribeiro, C. A. C. Souza, and J. C. C. Abrantes, "Use of Electrochemical Impedance Spectroscopy (EIS) to monitoring the corrosion of reinforced concrete," *Revista IBRACON de Estruturas e Materiais*, vol. 8, pp. 529–546, 2015. [Online]. Available: http://www.scielo.br/scielo.php?script=sci_arttext&pid=S1983-41952015000400529&nrm=iso
- [62] "Basics of Electrochemical Impedance Spectroscopy," 2020, <https://www.gamry.com/application-notes/EIS/basics-of-electrochemical-impedance-spectroscopy/>, last accessed on 11/11/2020.
- [63] M. E. Orazem, P. Agarwal, A. N. Jansen, P. T. Wojcik, and L. H. Garcia-Rubio, "Development of physico-chemical models for electrochemical impedance spectroscopy," *Electrochimica Acta*, vol. 38, no. 14, pp. 1903–1911, 1993. [Online]. Available: <http://www.sciencedirect.com/science/article/pii/0013468693803130>

- [64] P. Leuaa, D. Priyadarshani, A. K. Tripathi, and M. Neergat, "Internal and External Transport of Redox Species across the Porous Thin-Film Electrode/Electrolyte Interface," *Journal of Physical Chemistry C*, vol. 123, no. 35, pp. 21 440–21 447, 2019. [Online]. Available: <http://doi.org/10.1021/acs.jpcc.9b02795>
- [65] P. Leuaa, D. Priyadarshani, D. Choudhury, R. Maurya, and M. Neergat, "Resolving charge-transfer and mass-transfer processes of VO₂⁺/VO₂²⁺ redox species across the electrode/electrolyte interface using electrochemical impedance spectroscopy for vanadium redox flow battery," *RSC Adv.*, vol. 10, no. 51, pp. 30 887–30 895, 2020. [Online]. Available: <http://dx.doi.org/10.1039/D0RA05224H>
- [66] N. Mahato and M. M. Singh, "Investigation of Passive Film Properties and Pitting Resistance of AISI 316 in Aqueous Ethanoic Acid Containing Chloride Ions using Electrochemical Impedance Spectroscopy(EIS)," *Portugaliae Electrochimica Acta*, vol. 29, pp. 233–251, 2011. [Online]. Available: http://www.scielo.mec.pt/scielo.php?script=sci_{_}arttext{&}pid=S0872-19042011000400002{&}nrm=iso
- [67] "Quality of Your Fit in EIS," 2019, <https://www.gamry.com/application-notes/EIS/fit-in-eis/>, last accessed on 11/11/2020.
- [68] S. Pujiastuti and H. Onggo, "Effect of various concentration of sulfuric acid for Nafion membrane activation on the performance of fuel cell," *AIP Conference Proceedings*, vol. 1711, no. February 2016, 2016. [Online]. Available: <http://doi.org/10.1063/1.4941639>
- [69] T. Wang, S. J. Moon, D.-S. Hwang, H. Park, J. Lee, S. Kim, Y. M. Lee, and S. Kim, "Selective ion transport for a vanadium redox flow battery (VRFB) in nano-crack regulated proton exchange membranes," *Journal of Membrane Science*, vol. 583, pp. 16–22, 2019. [Online]. Available: <http://www.sciencedirect.com/science/article/pii/S0376738819300250>
- [70] M. Zago and A. Casalegno, "Physically-based impedance modeling of the negative electrode in All-Vanadium Redox Flow Batteries: insight into mass transport issues," *Electrochimica Acta*, vol. 248, no. July 2018, pp. 505–517. [Online]. Available: <https://doi.org/10.1016/j.electacta.2017.07.166>
- [71] M. Cecchetti, A. Casalegno, and M. Zago, "Local potential measurement through reference electrodes in vanadium redox flow batteries: Evaluation of overpotentials and electrolytes imbalance," *Journal of Power Sources*, vol. 400, no. August, pp. 218–224, 2018. [Online]. Available: <https://doi.org/10.1016/j.jpowsour.2018.08.033>
- [72] M. Nourani, B. I. Zackin, D. C. Sabarirajan, R. Taspinar, K. Artyushkova, F. Liu, I. V. Zenyuk, and E. Agar, "Impact of Corrosion Conditions on Carbon Paper Electrode Morphology and the

- Performance of a Vanadium Redox Flow Battery,” *Journal of The Electrochemical Society*, vol. 166, no. 2, pp. A353—A363, 2019. [Online]. Available: <https://doi.org/10.1149/2.1041902jes>
- [73] M. Becker and T. Turek, “Combination of impedance spectroscopy and potential probe sensing to characterize vanadium redox-flow batteries,” *Journal of Power Sources*, vol. 446, no. May 2019, p. 227349, 2020. [Online]. Available: <https://doi.org/10.1016/j.jpowsour.2019.227349>
- [74] H. Sun, M. Yu, Q. Li, K. Zhuang, J. Li, S. Almheiri, and X. Zhang, “Characteristics of charge/discharge and alternating current impedance in all-vanadium redox flow batteries,” *Energy*, vol. 168, pp. 693–701, 2019. [Online]. Available: <https://doi.org/10.1016/j.energy.2018.11.130>
- [75] J. L. Jespersen, A. E. Tønnesen, K. Nørregaard, L. Overgaard, and F. Elefsen, “Capacity Measurements of Li-Ion Batteries using AC Impedance Spectroscopy,” *World Electric Vehicle Journal*, vol. 3, pp. 127–133.
- [76] E. Hollmann, “Factors influencing kinetics of electrode processes in vanadium redox flow batteries,” *Chancellor’s Honors Program Projects*.
- [77] “Jerónimo Martins - CD Sul,” 2020, <https://engie-hemera.com/project/jeronimo-martins/>, last accessed on 02/12/2020.
- [78] “Investopedia,” 2020, <https://www.investopedia.com/>, last accessed on 01/12/2020.
- [79] M. J. Li, W. Zhao, X. Chen, and W. Q. Tao, “Economic analysis of a new class of vanadium redox-flow battery for medium- and large-scale energy storage in commercial applications with renewable energy,” *Applied Thermal Engineering*, vol. 114, pp. 802–814, 2017. [Online]. Available: <http://dx.doi.org/10.1016/j.applthermaleng.2016.11.156>
- [80] “Tarifários Disponíveis,” 2020, https://poupaenergia.pt/tarifarios/?offer_type=1&billing%5B0%5D=any&no_contract_duration=any, last accessed on 02/12/2020.
- [81] S. Kim, J. Yan, B. Schwenzer, J. Zhang, L. Li, J. Liu, Z. Yang, and M. A. Hickner, “Cycling performance and efficiency of sulfonated poly(sulfone) membranes in vanadium redox flow batteries,” *Electrochemistry Communications*, vol. 12, no. 11, pp. 1650–1653, 2010. [Online]. Available: <http://dx.doi.org/10.1016/j.elecom.2010.09.018>

